1 Present and future aerosol impacts on Arctic climate change in the GISS-E2.1 Earth system
2 model

4 Ulas Im[1,2,*], Kostas Tsigaridis[3,4], Gregory Faluvegi[3,4], Peter L. Langen[1,2], Joshua P. French[5],
5 Rashed Mahmood[6], Manu A. Thomas[7], Knut von Salzen[8], Daniel C. Thomas[1,2], Cynthia H.
6 Whaley[8], Zbigniew Klimont[9], Henrik Skov[1,2], Jørgen Brandt[1,2]
7
8 [1]Department of Environmental Science, Aarhus University, Roskilde, Denmark.
9 [2] Interdisciplinary Centre for Climate Change, Aarhus University, Roskilde, Denmark.
10 [3] Center for Climate Systems Research, Columbia University, New York, NY, USA.
11 [4] NASA Goddard Institute for Space Studies, New York, NY, USA.
12 [5] Department of Mathematical and Statistical Sciences, University of Colorado Denver, USA.
13 [6] Barcelona Supercomputing Center, Barcelona, Spain.
14 [7] Swedish Meteorological and Hydrological Institute, Norrköping, Sweden.
15 [8] Canadian Centre for Climate Modelling and Analysis, Environment and Climate Change Canada,
16 Victoria, British Columbia, Canada.
17 [9] International Institute for Applied Systems Analysis (IIASA), Laxenburg, Austria.
18 [*] Corresponding author

20 Abstract

22 The Arctic is warming two to three times faster than the global average, partly due to changes
23 in short-lived climate forcers (SLCFs) including aerosols. In order to study the effects of
24 atmospheric aerosols in this warming, recent past (1990-2014) and future (2015-2050)
25 simulations have been carried out using the GISS-E2.1 Earth system model to study the
26 aerosol burdens and their radiative and climate impacts over the Arctic (>60 °N), using
27 anthropogenic emissions from the Eclipse V6b and the Coupled Model Intercomparison
28 Project Phase 6 (CMIP6) databases, while global annual mean greenhouse gas concentrations
29 were prescribed and kept fixed in all simulations.
30
31 Results showed that the simulations have underestimated observed surface aerosol levels, in
32 particular black carbon (BC) and sulfate (SO_4^{2-}), by more than 50%, with the smallest biases
33 calculated for the atmosphere-only simulations, where winds are nudged to reanalysis data.
34 CMIP6 simulations performed slightly better in reproducing the observed surface aerosol
35 concentrations and climate parameters, compared to the Eclipse simulations. In addition,
36 simulations, where atmosphere and ocean are fully-coupled, had slightly smaller biases in
37 aerosol levels compared to atmosphere only simulations without nudging.
38
39 Arctic BC, organic aerosol (OA) and SO_4^{2-} burdens decrease significantly in all simulations
40 by 10-60% following the reductions of 7-78% in emission projections, with the CMIP6
41 ensemble showing larger reductions in Arctic aerosol burdens compared to the Eclipse
42 ensemble. For the 2030-2050 period, the Eclipse ensemble simulated a radiative forcing due
43 to aerosol-radiation interactions (RF_{ARI}) of -0.39±0.01 W m^{-2}, that is -0.08 W m^{-2} larger than
44 the 1990-2010 mean forcing (-0.32 W m^{-2}). of which -0.24±0.01 W m^{-2} were attributed to
45 the anthropogenic aerosols. The CMIP6 ensemble simulated a RF_{ARI} of -0.35 to -0. 40 W m^{-2}

46 for the same period, which is -0.01 to -0.06 W m^{-2} larger than the 1990-2010 mean forcing of
47 -0.35 W m^{-2}. The scenarios with little to no mitigation (worst-case scenarios) led to very
48 small changes in the RF$_{ARI}$, while scenarios with medium to large emission mitigations led to
49 increases in the negative RF$_{ARI}$, mainly due to the decrease of the positive BC forcing and the
50 decrease in the negative SO$_4^{2-}$ forcing. The anthropogenic aerosols accounted for -0.24 to -
51 0.26 W m^{-2} of the net RF$_{ARI}$ in 2030-2050 period, in Eclipse and CMIP6 ensembles,
52 respectively. Finally, all simulations showed an increase in the Arctic surface air
53 temperatures throughout the simulation period. By 2050, surface air temperatures are
54 projected to increase by 2.4 °C to 2.6 °C in the Eclipse ensemble and 1.9 °C to 2.6 °C in the
55 CMIP6 ensemble, compared to the 1990-2010 mean.
56
57 Overall, results show that even the scenarios with largest emission reductions leads to similar
58 impact on the future Arctic surface air temperatures and sea-ice extent compared to scenarios
59 with smaller emission reductions, implying reductions of greenhouse emissions are still
60 necessary to mitigate climate change.
61
62 1. Introduction
63
64 The Arctic is warming two to three times faster than the global average (IPCC, 2013;
65 Lenssen et al., 2019). This is partly due to internal Arctic feedback mechanisms, such as the
66 snow and sea-ice-albedo feedback, where melting ice leads to increased absorption of solar
67 radiation, which further enhances warming in the Arctic (Serreze and Francis, 2006).
68 However, Arctic temperatures are also affected by interactions with warming at lower
69 latitudes (e.g., Stuecker et al., 2018; Graversen and Langen, 2019; Semmler et al., 2020) and
70 by local in situ response to radiative forcing due to changes in greenhouse gases and aerosols
71 in the area (Shindell, 2007; Stuecker et al., 2018). In addition to warming induced by
72 increases in global atmospheric carbon dioxide (CO$_2$) concentrations, changes in short-lived
73 climate forcers (SLCFs) such as tropospheric ozone (O$_3$), methane (CH$_4$) and aerosols (e.g.
74 black carbon (BC) and sulfate (SO$_4^{2-}$)) in the Northern Hemisphere (NH), have contributed
75 substantially to the Arctic warming since 1890 (Shindell and Faluvegi, 2009; Ren et al.,
76 2020). This contribution from SLCFs to Arctic heating together with efficient local
77 amplification mechanisms puts a high priority on understanding the sources and sinks of
78 SLCFs at high latitudes and their corresponding climatic effects.
79
80 SLCFs include all atmospheric species, which have short residence times in the atmosphere
81 relative to long-lived greenhouse gases and have the potential to affect Earth's radiative
82 energy budget. Aerosols are important SLCFs and are a predominant component of air
83 quality that affects human health (Burnett et al., 2018, Lelieveld et al., 2019). They mostly
84 affect climate by altering the amount of solar energy absorbed by Earth, as well as changing
85 the cloud properties and indirectly affecting the scattering of radiation, and are efficiently
86 removed from the troposphere within several days to weeks. BC, which is a product of
87 incomplete combustion and open biomass/biofuel burning (Bond et al., 2004: 2013), absorbs
88 a high proportion of incident solar radiation and therefore warms the climate system
89 (Jacobson, 2001). SO$_4^{2-}$, which is formed primarily through oxidation of sulphur dioxide

90   (SO$_2$), absorbs negligible solar radiation and cools climate by scattering solar radiation back
91   to space. Organic carbon (OC), which is co-emitted with BC during combustion, both scatters
92   and absorbs solar radiation and therefore causes cooling in some environments and warming
93   in others. Highly reflective regions such as the Arctic are more likely to experience warming
94   effects from these organic aerosols (e.g., Myhre et al, 2013).

96   Aerosols also influence climate via indirect mechanisms. After being deposited on snow and
97   ice surfaces, BC can amplify ice melt by lowering the albedo and increasing solar heating of
98   the surface (AMAP, 2015). Aerosols also affect cloud properties, including their droplet size,
99   lifetime, and vertical extent, thereby influencing both the shortwave cooling and longwave
100   warming effects of clouds. Globally, this indirect cloud forcing from aerosols is likely larger
101   than their direct forcing, although the indirect effects are more uncertain and difficult to
102   accurately quantify (IPCC, 2013). Moreover, Arctic cloud impacts are distinct from global
103   impacts, owing to the extreme seasonality of solar radiation in the Arctic, unique
104   characteristics of Arctic clouds (e.g., high frequency of mixed-phase occurrence), and rapidly
105   evolving sea-ice distributions. Together, they lead to complicated and unique phenomena that
106   govern Arctic aerosol abundances and climate impacts (e.g., Willis et al., 2018; Abbatt et al.,
107   2019). The changes taking place in the Arctic have consequences for how SLCFs affect the
108   region. For example, reductions in sea-ice extent, thawing of permafrost, and humidification
109   of the Arctic troposphere can affect the emissions, lifetime and radiative forcing of SLCFs
110   within the Arctic (Thomas et al., 2019).

112   The effect of aerosols on the Arctic climate through the effects of scattering and absorption of
113   radiation, clouds, and surface ice/snow albedo has been investigated in previous studies (i.e.
114   Clarke and Noone, 1985; Flanner et al., 2007; Shindell et al., 2012; Bond et al., 2013;
115   Dumont et al., 2014). The impact of aerosols on the Arctic climate change is mainly driven
116   by a response to remote forcings (Gagné et al., 2015; Sand et al., 2015; Westervelt et al.,
117   2015). Long-range transport is known to play an important role in the Arctic air pollution
118   levels and much of the attention on aerosol climatic effects in the Arctic was focused on
119   long-range transported anthropogenic pollution (Arctic haze) in the past (Quinn et al., 2017;
120   AMAP, 2015; Abbatt et al., 2019). Long-range transport of BC and SO$_4^{2-}$, in particular from
121   Asia, travelling at a relatively high altitude to the Arctic, can be deposited on the snow and
122   ice, contributing to surface albedo reduction. On the other hand, there has been increasing
123   attention on the local Arctic aerosol sources, in particular natural aerosol sources (Schmale et
124   al., 2021). Lewinschal et al. (2019) estimated an Arctic surface temperature change per unit
125   global sulfur emission of -0.020 to -0.025 K per TgS yr^{-1}. Sand et al. (2020) calculated an
126   Arctic surface air temperature response of 0.06 - 0.1 K per Tg BC yr^{-1} to BC emissions in
127   Europe and North America, and slightly lower response (0.05-0.08 K per Tg BC yr^{-1}) to
128   Asian emissions. Breider et al. (2017) reported a short-wave (SW) aerosol radiative forcing
129   (ARF) of -0.19 ± 0.05 W m^{-2} at the top of the atmosphere (TOA) over the Arctic, which
130   reflects the balance between sulphate cooling (-0.60 W m^{-2}) and black carbon (BC) warming
131   ($+0.44$ W m^{-2}). Schacht et al. (2019) calculated a direct radiative forcing of up to 0.4 W m^{-2}
132   over the Arctic using the ECHAM6.3-HAM2.3 global aerosol-climate model. Markowicz et
133   al. (2021), using the NAAPS radiative transfer model, calculated the total aerosol forcing

134 over the Arctic (>70.5 °N) of -0.4 W m^{-2}. Ren et al. (2020) simulated 0.11 and 0.25 W m^{-2}
135 direct and indirect warning in 2014-2018 compared to 1980-1984 due to reductions in sulfate,
136 using the CAM5-EAST global aerosol-climate model. They also reported that the aerosols
137 produced an Arctic surface warming of +0.30 °C during 1980–2018, explaining about 20% of
138 the observed Arctic warming observed during the last four decades, while according to
139 Shindell and Faluvegi (2009), aerosols contributed 1.09 ± 0.81 °C to the observed Arctic
140 surface air temperature increase of 1.48 ± 0.28 °C observed in 1976-2007. AMAP (2015),
141 based on four ESMs, estimated a total Arctic surface air temperature response due to the
142 direct effect of current global combustion derived BC, OC and sulfur emissions to be +0.35
143 °C, of which +0.40 °C was attributed to BC in the atmosphere, +0.22 °C to BC in snow, -0.04
144 °C to OC and -0.23 °C to SO_4^{2-}. On the other hand, Stjern et al. (20117) and Takemura and
145 Suzuki (2019) showed that due to the rapid adjustments from BC, mitigation of BC emissions
146 can lead to weak responses in the surface temperatures. Samset et al. (2018), using a multi-
147 model ensemble of ocean coupled Earth system models (ESMs), where aerosol emissions
148 were either kept at present-day conditions, or anthropogenic emissions of SO_2, and fossil fuel
149 BC and OC were set to zero, showed that Arctic surface warming due to aerosol reductions
150 can reach up to 4°C in some locations, with a multi-model increase for the 60°N–90°N
151 region being 2.8°C. In addition, recent studies also suggest that as global emissions of
152 anthropogenic aerosols decrease, natural aerosol feedbacks may become increasingly
153 important for Arctic climate (Boy et al., 2019; Mahmood et al., 2019).
154
155 In this study, we carry out several simulations with the fully coupled NASA Goddard
156 Institute of Space Sciences (GISS) earth system model, GISS-E2.1 (Kelley et al., 2020) to
157 study the recent past and future burdens of aerosols as well as their impacts on TOA radiative
158 forcing and climate-relevant parameters such as surface air temperatures, sea-ice, and snow
159 over the Arctic (>60 °N). In addition, we investigate the impacts from two different emission
160 inventories; Eclipse V6b (Höglund-Isaksson et al.,2020; Klimont et al., 2021) vs. CMIP6
161 (Hoesly et al., 2018; van Marle et al., 2017: Feng et al.,2020), as well as differences between
162 atmosphere-only vs. fully-coupled simulations, on the evaluation of the model and the
163 climate impact. Section 2 introduces the GISS-E2.1 model, the anthropogenic emissions, and
164 the observation datasets used in model evaluation. Section 3 presents results from the model
165 evaluation as well as recent past and future trends in simulated aerosol burdens, radiative
166 forcing, and climate change over the Arctic. Section 4 summarizes the overall findings and
167 the conclusions.
168
169 2.   Materials and methods
170
171 2.1.   Model description
172
173 GISS-E2.1 is the CMIP6 version of the GISS modelE Earth system model, which has been
174 validated extensively over the globe (Kelly et al., 2020; Bauer et al., 2020) as well as
175 regionally for air pollutants (Turnock et al., 2020). A full description of GISS-E2.1 and
176 evaluation of its coupled climatology during the satellite era (1979–2014) and the recent past
177 ensemble simulation of the atmosphere and ocean component models (1850-2014) are

178 described in Kelly et al. (2020) and Miller et al. (2020), respectively. GISS-E2.1 has a
179 horizontal resolution of 2° in latitude by 2.5° in longitude and 40 vertical layers extending
180 from the surface to 0.1 hPa in the lower mesosphere. The tropospheric chemistry scheme
181 used in GISS-E2.1 (Shindell et al., 2013) includes inorganic chemistry of O_x, NO_x, HO_x, CO,
182 and organic chemistry of CH_4 and higher hydrocarbons using the CBM4 scheme (Gery et al.,
183 1989), and the stratospheric chemistry scheme (Shindell et al., 2013), which includes chlorine
184 and bromine chemistry together with polar stratospheric clouds.
185
186 In the present work, we used the One-Moment Aerosol scheme (OMA: Bauer et al., 2020 and
187 references therein), which is a mass-based scheme in which aerosols are assumed to remain
188 externally mixed. All aerosols have a prescribed and constant size distribution, with the
189 exception of sea salt that has two distinct size classes, and dust that is described by a
190 sectional model with an option from 4 to 6 bins. The default dust configuration that is used in
191 this work includes 5 bins, a clay and 4 silt ones, from submicron to 16 μm in size. The first
192 three dust size bins can be coated by sulfate and nitrate aerosols (Bauer & Koch, 2005). The
193 scheme treats sulfate, nitrate, ammonium, carbonaceous aerosols (black carbon and organic
194 carbon, including the NO_x-dependent formation of secondary organic aerosol (SOA) and
195 methanesulfonic acid formation), dust and sea-salt. The model includes secondary organic
196 aerosol production, as described by Tsigaridis and Kanakidou, (2007). SOA is calculated
197 from terpenes and other reactive volatile organic compounds (VOCs) using NOx-dependent
198 calculations of the 2-product model, as described in Tsigaridis and Kanakidou (2007).
199 Isoprene is explicitly used as a source, while terpenes and other reactive VOCs are lumped on
200 a-pinene, taking into account their different reactivity against oxidation. The semi-volatile
201 compounds formed can condense on all submicron particles except sea salt and dust. In the
202 model, an OA to OC ratio of 1.4 used. OMA only includes the first indirect effect, in which
203 the aerosol number concentration that impacts clouds is obtained from the aerosol mass as
204 described in (Menon & Rotstayn, 2006). The parameterization described by Menon and
205 Rotstayn (2006) that we use only affects the cloud droplet number concentration (CDNC),
206 not cloud droplet size, which is not explicitly calculated in GISS-E2.1. Following the change
207 in CDNC, we do not stop the model from changing either liquid water path (LWP) or
208 precipitation rates, since the clouds code sees the different CDNC and responds accordingly.
209 What we do not include is the 2nd indirect effect (autoconversion). In addition to OMA, we
210 have also conducted a non-interactive tracers (NINT: Kelley et al., 2020) simulation from
211 1850 to 2014, with noninteractive (through monthly varying) fields of radiatively active
212 components (ozone and multiple aerosol species) read in from previously calculated offline
213 fields from the OMA version of the model, ran using the Atmospheric Model
214 Intercomparison Project (AMIP) configuration in Bauer et al. (2020) as described in Kelley et
215 al. (2020). The NINT model includes a tuned aerosol first indirect effect following Hansen et
216 al. (2005).
217
218 The natural emissions of sea salt, dimethylsulfide (DMS), isoprene and dust are calculated
219 interactively. Anthropogenic dust sources are not represented in GISS-E2.1. Dust emissions
220 vary spatially and temporally only with the evolution of climate variables like wind speed
221 and soil moisture (Miller et al., 2006). The AMIP type simulations (see section 2.3) uses

prescribed sea surface temperature (SST) and sea ice fraction during the recent past (Rayner et al., 2003). The prescribed SST dataset in GISS-E2.1 is merged product based on the HadISST and NOAA Optimum Interpolation (OI) Sea Surface Temperature (SST) V2 (Reynolds et al., 2002).

2.2.   Emissions

In this study, we have used two different emission datasets; the ECLIPSE V6b (Höglund-Isaksson et al.,2020; Klimont et al., 2021), which has been developed with support of the EU-funded Action on Black Carbon in the Arctic (EUA-BCA) and used in the framework of the ongoing AMAP Assessment (AMAP, 2021), referred to as *Eclipse* in this paper, and the CEDS emissions (Hoesly et al., 2018; Feng et al.,2020) combined with selected Shared Socio-economic Pathways (SSP) scenarios used in the CMIP6 future projections (Eyring et al., 2016), collectively referred to as *CMIP6* in this paper.

2.2.1. EclipseV6b emissions

The ECLIPSE V6b emissions dataset is a further evolution of the scenarios established in the EU funded ECLIPSE project (Stohl et al., 2015; Klimont et al., 2017). It has been developed with the global implementation of the GAINS (Greenhouse gas – Air pollution Interactions and Synergies) model (Amann et al., 2011). The GAINS model includes all key air pollutants and Kyoto greenhouse gases, where emissions are estimated for nearly 200 country-regions and several hundred source-sectors representing anthropogenic emissions. For this work, annual emissions were spatially distributed on 0.5°x0.5° lon-lat grids for nine sectors: energy, industry, solvent use, transport, residential combustion, agriculture, open burning of agricultural waste, waste treatment, gas flaring and venting, and international shipping. A monthly pattern for each gridded layer was provided at a 0.5°x0.5° grid level. The ECLIPSE V6b dataset, used in this study, includes an estimate for 1990 to 2015 using statistical data and two scenarios extending to 2050 that rely on the same energy projections from the World Energy Outlook 2018 (IEA, 2018) but have different assumptions about the implementation of air pollution reduction technologies, as described below.

The Current Legislation (CLE) scenario assumes efficient implementation of the current air pollution legislation committed before 2018, while the Maximum Feasible Reduction (MFR) scenario assumes implementation of best available emission reduction technologies included in the GAINS model. The MFR scenario demonstrates the additional reduction potential of SO_2 emissions by up to 60% and 40%, by 2030 for Arctic Council member and observer countries respectively, with implementation of best available technologies mostly in the energy and industrial sectors and to a smaller extent via measures in the residential sector. The Arctic Council member countries' maximum reduction potential could be fully realized by 2030 whereas in the observer countries additional reductions of 15% to 20% would remain to be achieved between 2030 and 2050. The assumptions and the details for the CLE and MFR scenarios (as well as other scenarios developed within the ECLIPSE V6b family) can be found in Höglund-Isaksson et al. (2020) and Klimont et al. (in preparation).

2.2.2. CMIP6 emissions

The CMIP6 emission datasets include a historical time series generated by the Community Emissions Data System (CEDS) for anthropogenic emissions (Hoesly et al., 2018; Feng et al., 2020), open biomass burning emissions (van Marle et al., 2010), and the future emission scenarios driven by the assumptions embedded in the Shared Socioeconomic Pathways (SSPs) and Representative Concentration Pathways (RCPs) (Riahi et al., 2017) that include specific air pollution storylines (Rao et al., 2017). Gridded CMIP6 emissions are aggregated to nine sectors: agriculture, energy, industrial, transportation, residential–commercial–other, solvents, waste, international shipping, and aircraft. SSP data for future emissions from integrated assessment models (IAMs) are first harmonized to a common 2015 base-year value by the native model per region and sector. This harmonization process adjusts the native model data to match the 2015 starting year values with a smooth transition forward in time, generally converging to native model results (Gidden et al., 2018). The production of the harmonized future emissions data is described in Gidden et al. (2019).

2.2.3. Implementation of the emissions in the GISS-E2.1

The Eclipse V6b and CEDS emissions on $0.5° \times 0.5°$ spatial resolution are regridded to $2° \times 2.5°$ resolution in order to be used in the various GISS-E2.1 simulations. In the GISS-E2.1 Eclipse simulations, the non-methane volatile organic carbons (NMVOC) emissions are chemically speciated assuming the SSP2-4.5 VOC composition profiles. In the Eclipse simulations, biomass burning emissions are taken from the CMIP6 emissions, which have been pre-processed to include the agricultural waste burning emissions from the EclipseV6b dataset, while the rest of the biomass burning emissions are taken as the original CMIP6 biomass burning emissions. In addition to the biomass burning emissions, the aircraft emissions are also taken from the CMIP6 database to be used in the Eclipse simulations. As seen in Figure 1, the emissions are consistently higher in the CMIP6 compared to the Eclipse emissions. The main differences in the two datasets are mainly over south-east Asia (not shown) . The CMIP6 emissions are also consistently higher on a sectoral basis compared to the Eclipse emissions. The figure shows that for air pollutant emissions, the CMIP6 SSP1-2.6 scenario and the Eclipse MFR scenario follow each other closely, while the Eclipse CLE scenario is comparable with the CMIP6 SSP2-4.5 scenario for most pollutants; that is to some extent owing to the fact that the CO_2 trajectory of the Eclipse CLE and the SSP2-4.5 are very similar (not shown). A more detailed discussion of differences between historical Eclipse and CMIP6 as well as CMIP6 scenarios are provided in Klimont et al. (in preparation).

2.3. Simulations

In order to contribute to the AMAP Assessment report (AMAP, 2021), the GISS-E2.1 model participated with AMIP-type simulations, which aim to assess the trends of Arctic air pollution and climate change in the recent past, as well as with fully-coupled climate simulations. Five fully-coupled Earth system models (ESMs) simulated the future (2015-2050) changes of atmospheric composition and climate in the Arctic (>60°N), as well as over

the globe. We have carried out two AMIP-type simulations, one with winds nudged to NCEP (standard AMIP-type simulation in AMAP) and one with freely varying winds, where both simulations used prescribed SSTs and sea-ice (Table 1). In the fully-coupled simulations, we carried out two sets of simulations, each with three ensemble members, that used the CLE and MFR emission scenarios. Each simulation in these two sets of scenarios were initialized from a set of three fully-coupled ensemble recent past simulations (1990-2014) to ensure a smooth continuation from CMIP6 to Eclipse emissions.

In addition to the AMAP simulations, we have also conducted CMIP6-type simulations in order to compare the climate aerosol burdens and their impacts on radiative forcing and climate impacts with those from the AMAP simulations. We have used the SSP1-2.6, 2-4.5, 3-7.0, and 3-7.0-lowNTCF scenarios representing different levels of emission mitigations in the CMIP6 simulations. SSP1 and SSP3 define various combinations of high or low socio-economic challenges to climate change adaptation and mitigation, while SSP2 describes medium challenges of both kinds and is intended to represent a future in which development trends are not extreme in any of the dimensions, but rather follow middle-of-the-road pathways (Rao et al., 2017). SSP1-2.6 scenario aims to achieve a 2100 radiative forcing level of 2.6 W m^{-2}, keeping the temperature increase below 2 °C compared to the preindustrial levels. The SSP2-4.5 describes a "middle of the road" socio-economic family with a 4.5 W m^{-2} radiative forcing level by 2100. The SSP3- 7.0 scenario is a medium-high reference scenario. SSP3-7.0-lowNTCF is a variant of the SSP3-7.0 scenario with reduced near-term climate forcer (NTCF) emissions. The SSP3-7.0 scenario has the highest methane and air pollution precursor emissions, while SSP3-7.0-lowNTCF investigates an alternative pathway for the Aerosols and Chemistry Model Intercomparison Project (AerChemMIP: Collins et al., 2017), exhibiting very low methane, aerosol, and tropospheric-ozone precursor emissions – approximately in line with SSP1-2.6. As seen in Table 1, we have conducted one transient fully-coupled simulation from 1850 to 2014, and a number of future scenarios.

We have employed prescribed global and annual mean greenhouse (CO_2 and CH_4) concentrations, where a linear increase in global mean temperature of 0.2 °C/decade from 2019 to 2050 was assumed, which are approximately in line with the simulated warming rates for the SSP2-4.5 scenario (AMAP, 2021).

2.4.   Observations

The GISS-E2.1 ensemble has been evaluated against surface observations of BC, organic aerosols (sum of OC and secondary organic aerosols (SOA), referred as OA in the rest of the paper) and SO_4^{2-}, ground-based and satellite-derived AOD 550 nm, as well as surface and satellite observations of surface air temperature, precipitation, sea surface temperature, sea-ice extent, cloud fraction, and liquid and ice water content in 1995-2014 period. The surface monitoring stations used to evaluate the simulated aerosol levels have been listed in Table S1 and S2 in the supplementary materials.

2.4.1. Aerosols

350

351 Measurements of speciated particulate matter (PM), BC, SO_4^{2-}, and (OA) come from three
352 major networks: the Interagency Monitoring of Protected Visual Environments (IMPROVE)
353 for Alaska (The IMPROVE measurements that are in the Arctic (>60°N) are all in Alaska);
354 the European Monitoring and Evaluation Programme (EMEP) for Europe; and the Canadian
355 Air Baseline Measurements (CABM) for Canada (Table S1 and S2). In addition to these
356 monitoring networks, BC, OA, and SO_4^{2-} measurements from individual Arctic stations were
357 used in this study. The individual Arctic stations are Fairbanks and Utqiagvik, Alaska (part of
358 IMPROVE, though their measurements were obtained from their PIs); Gruvebadet and
359 Zeppelin mountain (Ny Alesund), Norway; Villum Research Station, Greenland; and Alert,
360 Nunavut (the latter being an observatory in Global Atmospheric Watch-WMO, and a part of
361 CABM). The measurement techniques are briefly described in the supplement.

362

363 AOD at 500 nm from the AErosol RObotic NETwork (AERONET, Holben et al., 1998) was
364 interpolated to 550 nm AOD using the Ångström formula (Ångström, 1929). We also used a
365 new merged AOD product developed by Sogacheva et al. (2020) using AOD from 10
366 different satellite-based products. According to Sogacheva et al. (2020), this merged product
367 could provide a better representation of temporal and spatial distribution of AOD. However,
368 it is important to note that the monthly aggregates of observations for both AERONET and
369 the satellite products depend on availability of data and are not likely to be the true aggregate
370 of observations for a whole month when only few data points exist during the course of a
371 month. In addition, many polar orbiting satellites take one observation during any given day,
372 and typically at the same local time. Nevertheless, these data sets are key observations
373 currently available for evaluating model performances. Information about the uncertain
374 nature of AOD observations can be found in previous studies (e.g. Sayer et al., 2018; Sayer
375 and Knobelspiesse, 2019; Wei et al., 2019; Schutgens et al., 2020, Schutgens, 2020;
376 Sogacheva et al., 2020).

377

378 *2.4.2. Surface air temperature, precipitation, and sea-ice*

379

380 Surface air temperature and precipitation observations used in this study are from University
381 of Delaware gridded monthly mean data sets (UDel; Willmott and Matsuura, 2001). UDel's
382 0.5° resolution gridded data sets are based on interpolations from station-based measurements
383 obtained from various sources including the Global Historical Climate Network, the archive
384 of Legates and Willmott and others. The Met Office Hadley Center's sea ice and sea surface
385 temperature (HadISST; Rayner et al., 2003) was used for evaluating model simulations of sea
386 ice and SSTs. HadISST data is an improved version of its predecessor known as global sea
387 ice and sea surface temperature (GISST). HadISST data is constructed using information
388 from a variety of data sources such as the Met Office Marine Database, Comprehensive
389 Ocean-Atmosphere Data Set, passive microwave remote sensing retrieval and sea ice charts.

390

391 *2.4.3. Satellite observations used for cloud fraction and cloud liquid water and ice water*

392

393 The Advanced Very High Resolution Radiometer (AVHRR-2) sensors onboard the NOAA
394 and EUMETSAT polar orbiting satellites have been flying since the early 1980s. These data
395 have been instrumental in providing the scientific community with climate data records
396 spanning nearly four decades. Tremendous progress has been made in recent decades in
397 improving, training and evaluating the cloud property retrievals from these AVHRR sensors.
398 In this study, we use the retrievals of total cloud fraction from the second edition of
399 EUMETSATs Climate Monitoring Satellite Application Facility (CM SAF) Cloud, Albedo
400 and surface Radiation data set from AVHRR data (CLARA-A2, Karlsson et al., 2017). This
401 cloud property climate data record is available for the period 1982-2018. Its strengths and
402 weaknesses and inter-comparison with the other similar climate data records are documented
403 in Karlsson and Devasthale (2018). Further data set documentation including Algorithm
404 Theoretical Basis and Validation reports can be found in Karlsson et al. (2017).
405
406 Cloud liquid and ice water path estimates derived from the cloud profiling radar on board
407 CloudSat (Stephens et al., 2002) and constrained with another sensor onboard NASA's A-
408 Train constellation, MODIS-Aqua (Platnick et al., 2015), are used for the model evaluation.
409 These Level 2b retrievals, available through 2B-CWC-RVOD product (Version 5), for the
410 period 2007-2016 are analysed. This constrained version is used instead of its radar-only
411 counterpart, as it uses additional information about visible cloud optical depths from MODIS,
412 leading to better estimates of cloud liquid water paths. Because of this constraint the data are
413 available only for the day-lit conditions, and hence, are missing over the polar regions during
414 the respective winter seasons. The theoretical basis for these retrievals can be found in
415 http://www.cloudsat.cira.colostate.edu/sites/default/files/products/files/2B-CWC-
416 RVOD_PDICD.P1_R05.rev0_.pdf (last access: October 26th 2020). Being an active cloud
417 radar, CloudSat provides orbital curtains with a swath width of just about 1.4 km. Therefore,
418 the data are gridded at 5°x5° to avoid too many gaps or patchiness and to provide robust
419 statistics.
420
421 3.   Results
422
423 3.1.   Evaluation
424
425 The simulations are compared against surface measurements of BC, OA, SO_4^{2-} and AOD, as
426 well as surface and satellite measurements of surface air temperature, precipitation, sea
427 surface temperature, sea-ice extent, total cloud fraction, liquid water path, and ice water path
428 described in section 2.4, by calculating the correlation coefficient (*r*) and normalized mean
429 bias (*NMB*). OA refers to the sum of primary organic carbon (OC) and secondary organic
430 aerosols (SOA).
431
432 *3.1.1. Aerosols*
433 The recent past simulations are for BC, OA, SO_4 and AOD (Table 2) against available
434 surface measurements. The monthly observed and simulated time series for each station are
435 accumulated per species in order to get a full Arctic timeseries data, which also includes
436 spatial variation, to be used for the evaluation of the model. In addition to Table 2, the

437 climatological mean (1995-2014) of the observed and simulated monthly surface
438 concentrations of BC, OA, SO_4^{2-} and AOD at 550 nm (note that AOD is averaged over 2008,
439 2009 and 2014) are shown in Figure 2. The AOD observation data for years 2008, 2009, and
440 2014 are used in order to keep the comparisons in line with the multi-model evaluations
441 being carried out in the AMAP assessment report (AMAP, 2021). We also provide spatial
442 distributions of the NMB, calculated as the mean of all simulations for BC, OA, SO_4 and
443 AOD in Figure 3. The statistics for the individual stations are provided in the Supplementary
444 Material, Tables S3-S6.

446 Results showed overall an underestimation of aerosol species over the Arctic, as discussed
447 below. Surface BC levels are underestimated at all Arctic stations from 15% to 90%. Surface
448 OA levels are also underestimated from -5% to -70%, except for a slight overestimation of
449 <1% over Karvatn (B5) and a large overestimation of 90% over Trapper Creek (B6). Surface
450 SO_4^{2-} concentrations are also consistently underestimated from -10% to -70%, except for
451 Villum Research Station (S11) over northeastern Greenland where there is an overestimation
452 of 45%. Finally, AODs are also underestimated over all stations from 20% to 60%. Such
453 underestimations at high latitudes have also been reported by many previous studies (e.g.
454 Skeike et al., 2011; Eckhardt et al., 2015; Lund et al., 2017, 2018; Schacht et al., 2019;
455 Turnock et al., 2020), pointing to a variety of reasons including uncertainties in emission
456 inventories, errors in the wet and dry deposition schemes, the absence or underrepresentation
457 of new aerosol formation processes, and the coarse resolution of global models leading to
458 errors in emissions and simulated meteorology, as well as in representation of point
459 observations in coarse model grid cells. Turnock et al. (2020) evaluated the air pollutant
460 concentrations in the CMIP6 models, including the GISS-E2.1 ESM, and found that observed
461 surface $PM_{2.5}$ concentrations are consistently underestimated in CMIP6 models by up to 10
462 $\mu g\ m^{-3}$, particularly for the Northern Hemisphere winter months, with the largest model
463 diversity near natural emission source regions and the Polar regions.

465 The BC levels are largely underestimated in simulations by 50% (CMIP6_Cpl_Hist) to 67%
466 (Eclipse_AMIP). The CMIP6 simulations have lower bias compared to EclipseV6b
467 simulations due to higher emissions in the CMIP6 emission inventory (Figure 1). Within the
468 EclipseV6b simulations, the lowest bias (-57%) is calculated for the Eclipse_AMIP_NCEP
469 simulation, while the free climate and coupled simulations showed a larger underestimation
470 (>62%), which can be attributed to a better simulation of transport to the Arctic when nudged
471 winds are used. The Eclipse simulations also show that the coupled simulations had slightly
472 smaller biases (*NMB*=-63%) compared to the AMIP-type free climate simulation (AMIP-
473 OnlyAtm: *NMB*=-67%). The climatological monthly variation of the observed levels is
474 poorly reproduced by the model with *r* values around 0.3. BC levels are mainly
475 underestimated in winter and spring, which can be attributed to the underestimation of the
476 anthropogenic emissions of BC, while the summer levels are well captured by the majority of
477 the simulations (Figure 2).

479 Surface OA concentrations are underestimated from 8% (Eclipse_AMIP_NCEP) to 35%
480 (Eclipse_AMIP) by the Eclipse ensemble, while the CMIP6_Cpl_Hist simulation

481 overestimated surface OA by 13%. The Eclipse simulations suggest that the nudged winds
482 lead to a better representation of transport to the Arctic, while the coupled simulations had
483 smaller biases compared to the AMIP-type free climate simulation (AMIP-OnlyAtm), similar
484 to BC. The climatological monthly variation of the observed concentrations are reasonably
485 simulated, with r values between 0.51 and 0.69 (Table 2 and Figure 2). As can be seen in
486 Figure S1, the OA levels are dominated by the biogenic SOA, in particular via α-pinene
487 (monoterpenes) oxidation, compared to anthropogenic (by a factor of 4-9) and biomass
488 burning (by a factor of 2-3) OA. While OC and BC are emitted almost from similar sources,
489 this biogenic-dominated OA seasonality also explains why simulated BC seasonality is not as
490 well captured, suggesting the underestimations in the anthropogenic emissions of these
491 species, in particular during the winter.
492
493 Surface SO_4^{2-} levels are simulated with a smaller bias compared to the BC levels, however
494 still underestimated by 40% (CMIP6_Cpl_Hist) to 53% (Eclipse_AMIP_NCEP). The
495 Eclipse_AMIP_NCEP simulation is biased higher (NMB=-53%) compared to the
496 Eclipse_AMIP (NMB=-50%), probably due to higher cloud fraction simulated by the nudged
497 version (see section 3.1.6), leading to higher in-cloud SO_4^{2-} production. The climatological
498 monthly variation of observed SO_4^{2-} concentrations are reasonably simulated in all
499 simulations (r=0.65-0.74). The observed springtime maximum is well captured by the GISS-
500 E2.1 ensemble, with underestimations in all seasons, mainly suggesting underestimations in
501 anthropogenic SO_2 emissions (Figure 2), as well as simulated cloud fractions, which have
502 high positive bias in winter and transition seasons, while in summer, the cloud fraction is well
503 captured with a slight underestimation. The clear sky AOD over the Aeronet stations in the
504 Arctic region is underestimated by 33% (Eclipse_AMIP) to 47% (Eclipse_CplHist1). Similar
505 negative biases are found with comparison to the satellite based AOD product (Table 2). The
506 climatological monthly variation is poorly captured with r values between -0.07 to 0.07
507 compared to AERONET AOD and 0 to 0.13 compared to satellite AOD. The simulations
508 could not represent the climatological monthly variation of the observed AERONET AODs
509 (Figure 2).
510
511 *3.1.2. Climate*
512 The different simulations are evaluated against a set of climate variables and the statistics are
513 presented in Table 3a and 3b, and in Figures 4 and 5. The climatological mean (1995-2014)
514 monthly Arctic surface air temperatures are slightly overestimated by up to 0.55 °C in the
515 AMIP simulations, while the coupled ocean simulations underestimate the surface air
516 temperatures by up to -0.17 °C. All simulations were able to reproduce the monthly
517 climatological variation with r values of 0.99 and higher (Figure 4). Results show that both
518 absorbing (BC) and scattering aerosols (OC and SO_4^{2-}) are underestimated by the GISS-E2.1
519 model, implying that these biases can partly cancel out their impacts on radiative forcing due
520 to aerosol-radiation interactions. This, together with the very low biases in surface
521 temperatures suggests that aerosols over the Arctic do not affect the Arctic climate and that
522 the changes in Arctic climate are mainly driven by changes due to greenhouse gas
523 concentrations. The monthly mean precipitation has been underestimated by around 50% by
524 all simulations (Table 3a), with largest biases during the summer and autumn (Figure 4). The

525 observed monthly climatological mean variation was very well simulated by all simulations,
526 with r values between 0.80 and 0.90.
527
528 Arctic SSTs are underestimated by the ocean-coupled simulation up to -1.96 °C, while the
529 atmosphere-only runs underestimated SSTs by -1.5 °C (Table 3a). This difference is
530 attributed to the differences in the SST data used as model input (Reynolds et al., 2002) and
531 data used to evaluate the model (Rayner et al., 2003). The monthly climatological mean
532 variation is well captured with r values above 0.99 (Table 3a, Figure 4), with a similar cold
533 bias in almost all seasons. The sea-ice extent was overestimated by all coupled simulations by
534 about 12%, while the AMIP-type Eclipse simulations slightly underestimated the extent by
535 3% (Table 3a). The observed variation was also very well captured with very high r values.
536 The winter and spring biases were slightly higher compared to the summer and autumn biases
537 (Figure 4).
538
539 All simulations overestimate the climatological (1995-2014) mean total cloud fraction by
540 21% to 25% during the extended winter months (October through February), where the
541 simulated seasonality is anti-correlated in comparison to AVHRR CLARA-A2 observations,
542 whereas, a good correlation is seen during the summer months irrespective of the
543 observational data reference. The largest biases were simulated by the atmosphere-only
544 simulations, with the nudged simulation having the largest bias (NMB=25%). The coupled
545 model simulations are closer to the observations during the recent past. On the other hand, the
546 climatology of the annual-mean cloud fraction was best simulated by the nudged atmosphere-
547 only simulation (Eclipse_AMIP_NCEP) with a r value of 0.40, while other simulations
548 showed a poor performance (r=-0.17 to +0.10), except for the summer where the bias is
549 lowest (Figure 5). The evaluation against CALIPSO data however shows much smaller biases
550 (NMB = +3% to +6%). This is because in comparison to CALIPSO satellite that carries an
551 active lidar instrument (CALIOP), the CLARA-A2 dataset has difficulties in separating cold
552 and bright ice/snow surfaces from clouds thereby underestimating the cloudiness during
553 Arctic winters. Here both datasets are used for the evaluation as they provide different
554 observational perspectives and cover the typical range of uncertainty expected from the
555 satellite observations. Furthermore, while the CLARA-A2 covers the entire evaluation period
556 in current climate scenario, CALIPSO observations are based on 10-year data covering the
557 2007-2016 period.
558
559 Figure 5 shows the evaluation of the simulations with respect to LWP and IWP. It has to be
560 noted here that to obtain a better estimate of the cloud water content, the CloudSat
561 observations were constrained with MODIS observations which resulted in a lack of data
562 during the months with darkness (Oct-Mar) over the Arctic (see Section 2.4.3). Hence, we
563 present the results for the polar summer months only. As seen in Figure 5, all simulations
564 overestimated the climatological (2007-2014) mean Polar summer LWP by up to almost
565 75%. The smallest bias (14%) is calculated for the nudged atmosphere-only
566 (Eclipse_OnlyAtm_NCEP), while the coupled simulations had biases of 70% or more.
567 Observations show a gradual increase in the LWP, peaking in July, whereas the model
568 simulates a more constant amount for the nudged simulation and a slightly decreasing

569 tendency for the other configurations. All model simulations overestimate LWP during the
570 spring months. The atmosphere-only nudged simulations tend to better simulate the observed
571 LWP during the summer months (June through September). The coupled simulations,
572 irrespective of the emission dataset used, are closer to observations only during the months of
573 July and August.
574
575 The climatological (2007-2014) mean Polar summer IWP is slightly better simulated
576 compared to the LWP, with biases within -60% with the exception of the nudged Eclipse
577 (Eclipse_AMIP_NCEP) simulation (NMB=-74%). All simulations simulated the monthly
578 variation well, with r values of 0.95 and more.
579
580 In the Arctic, the net cloud forcing at the surface changes sign from positive to negative
581 during the polar summer (Kay and L'Ecuyer, 2013). This change typically occurs in May
582 driven mainly by shortwave cooling at the surface. Since the model simulates the magnitude
583 of the LWP reasonably, particularly in summer, the negative cloud forcing can also be
584 expected to be realistic in the model (e.g. Gryspeerdt et al. 2019). Furthermore, the aerosol
585 and pollution transport into the Arctic typically occurs in the lowermost troposphere where
586 liquid water clouds are prevalent during late spring and summer seasons. The interaction of
587 ice clouds with aerosols is, however, more complex, as ice clouds could have varying optical
588 thicknesses, with mainly thin cirrus in the upper troposphere and relatively thicker clouds in
589 the layers below. Without the knowledge on the vertical distribution of optical thickness, it is
590 difficult to infer the potential impact of the underestimation of IWP on total cloud forcing and
591 their implications.
592
593 3.2. Arctic burdens and radiative forcing due to aerosol-radiation interactions (RF$_{ARI}$)
594
595 The recent past and future Arctic column burdens for BC, OA and SO$_4^{2-}$ for the different
596 scenarios and emissions are provided in Figure 6. In addition, Table 4 shows the calculated
597 trends in the burdens for BC, OA and SO$_4^{2-}$ for the different scenarios, while Table 5
598 provides the 1990-2010 and 2030-2050 mean burdens of the aerosol components. The BC
599 and SO$_4^{2-}$ burdens started decreasing from the 1990s, while OA burden remains relatively
600 constant, although there is large year-to-year variability in all simulations. All figures show a
601 decrease in burdens after 2015, except for the SSP3-7.0 scenario, where the burdens remain
602 close to the 2015 levels. The high variability in BC and OA burdens over the 2000's is due to
603 the biomass burning emissions from GFED, which have not been harmonized with the no-
604 satellite era. It should also be noted that these burdens can be underestimated considering the
605 negative biases calculated for the surface concentrations and in particular for the AODs
606 reported in Table 2 and Tables S2-6.
607
608 In addition to the burdens of these aerosol species, the TOA radiative forcing due to aerosol-
609 radiation interaction (RF$_{ARI}$) over the Arctic are simulated by the GISS-E2.1 ensemble. RF$_{ARI}$
610 is calculated as the sum of shortwave and longwave forcing from the individual aerosol
611 species between 1850 and 2050 are presented in Figure 7. The instantaneous forcings are
612 calculated with a double call to the model's radiation code, with and without aerosols. The

613   model outputs separate forcing diagnostics for anthropogenic and biomass burning BC and
614   OC, as well as biogenic SOA, making it possible to attribute the forcing to individual aerosol
615   species. The negative RF_{ARI} has increased significantly since 1850 until the 1970's due to an
616   increase in aerosol concentrations. Due to the efforts of mitigating air pollution and thus a
617   decrease in emissions, the forcing became less negative after the 1970's until 2015. Figure 7
618   also shows a visible difference in the anthropogenic RF_{ARI} simulated by the NINT
619   (prescribed aerosols) and OMA (interactive aerosols) simulations in the CMIP6 ensemble,
620   where the anthropogenic RF_{ARI} by NINT simulation is less negative (by almost 30%)
621   compared to the OMA simulation (Figure 7b). On the other hand, no such difference is seen
622   in the net RF_{ARI} time series (Figure 7a). This compensation is largely driven by the 50% more
623   positive dust and 10% less negative sea-salt RF_{ARI} in the OMA simulation.
624

625   *3.2.1. Black carbon*
626   All simulations show a statistically significant (as calculated by Mann-Kendall trend
627   analyses) decrease in the Arctic BC burdens (Table 4) between 1990-2014, except for the
628   CMIP6_Cpl_Hist, which shows a slight non-significant increase that can be attributed to the
629   large increase in global anthropogenic BC emissions in CMIP6 after year 2000 (Figure 1).
630   From 2015 onwards, all future simulations show a statistically significant decrease in the
631   Arctic BC burden (Table 4). The Eclipse CLE ensemble shows a 1.1 kTon (31%) decrease in
632   the 2030-2050 mean Arctic BC burden compared to the 1990-2010 mean, while the decrease
633   in 2030-2050 mean Arctic BC burden is larger in the MFR ensemble (2.3 kTon: 62%). In the
634   CMIP6 simulations, the 2030-2050 mean Arctic BC burdens decrease by 0.70 to 1.59 kTon,
635   being largest in SSP1-2.6 and lowest in SSP3-7.0-lowNTCF, while the SSP3-7.0 simulation
636   leads to an increase of 0.43 kTon (12%) in 2030-2050 mean Arctic BC burdens. It is
637   important to note that the changes in burden simulated by the Eclipse CLE ensemble (-1.1
638   kTon) is comparable with the change of -1 kTon in the SSP2-4.5 scenario, consistent with the
639   projected emission changes in the two scenarios (Figure 1).
640

641   As seen in Table 6, the GISS-E2.1 ensemble calculated a BC RF_{ARI} of up to 0.23 W m^{-2} over
642   the Arctic, with both CMIP6 and Eclipse coupled simulations estimating the highest forcing
643   of 0.23 W m^{-2} for the 1990-2010 mean (Table 6a). This agrees with previous estimates of the
644   BC RF_{ARI} over the Arctic (e.g. Schacht et al., 2019). In the future, the positive BC RF_{ARI} is
645   generally decreasing (Figure 6) due to lower BC emissions, except for the SSP3-7.0 scenario,
646   where the BC forcing becomes more positive by 0.05 W m^{-2}. The changes in the Arctic RF_{ARI}
647   in Table 6a follows the Arctic burdens presented in Table 5, and emission projections
648   presented in Figure 1, leading to largest reductions in BC RF_{ARI} simulated in SSP1-2.6 (-0.10
649   Wm^{-2}). Similar to the burdens, the Eclipse CLE and CMIP6 SSP2-4.5 scenarios simulate a
650   very close decrease in the 2030-2050 mean BC RF_{ARI} of -0.06 Wm^{-2} and -0.06 Wm^{-2},
651   respectively.
652

653   *3.2.2. Organic aerosols*
654   The Eclipse historical ensemble simulate a positive OA burden trend between 1990 and 2014,
655   however this trend is not significant at the 95% confidence level (Table 4). The
656   CMIP6_Cpl_Hist simulation gives a larger trend, due to a large increase in global

657 anthropogenic OC emissions in CMIP6 (Figure 1). The nudged AMIP Eclipse simulation
658 calculates the largest 1990-2010 mean OA burden (57 kTon), while the coupled simulation
659 shows a slightly lower 1990-2010 mean burden (55 kTon). This largest OA burden in the
660 Eclipse_AMIP_NCEP simulation is attributed to the largest biogenic SOA burden calculated
661 in this scenario, as well as a better-simulated transport from source regions due to the nudged
662 winds (Figure S1). The anthropogenic and biogenic contributions to SOA burdens in the
663 coupled Eclipse and CMIP6 recent past simulations imply that the differences in the burdens
664 between the two ensembles can be attributed to the different anthropogenic emissions
665 datasets used in the Eclipse and CMIP6 simulations (Figure S1), as well as the differences in
666 SOA contributions due to simulated increases in the biogenic emissions (Figure S5) . The
667 AMIP-type Eclipse run simulates a lower 1990-2010 mean OA burden (50 kTon), attributed
668 to the smallest biogenic SOA burden in this scenario. The Eclipse CLE ensemble shows a
669 decrease of 6.6 kTon (12%) in 2030-2050 mean OA burden compared to the 1990-2010
670 mean, while the MFR ensemble shows a larger decrease in the same period (15.2 kTon:
671 27%). The CMIP6 simulations show a much larger decrease of 2030-2050 mean Arctic OA
672 burdens, with a decrease of 8.1 kTon (SSP2-4.5) to 17 kTon (SSP1-2.6), while the SSP3-7.0
673 simulation shows an increase in OA burdens in the same period by 1.3 kTon (2%). Similar to
674 BC burdens, Eclipse CLE and CMIP6 SSP2-4.5 scenarios project similar changes in 2030-
675 2050 mean OA burden (6.6 kTon and 8.1 kTon, respectively).

676

677 As shown in Table 6a, the Eclipse ensemble calculated an OA RF_{ARI} of -0.05 to -0.08 Wm^{-2}
678 for the 1990-2010 mean, where the nudged AMIP-type simulation shows the largest RF_{ARI},
679 due to the largest Arctic OA burden calculated for this period (Table 5). For the future, both
680 Eclipse CLE and MFR ensembles show an increase in the negative 2030-2050 mean RF_{ARI}
681 by -0.02 Wm^{-2}, which is very close to the increase in the negative forcing calculated for the
682 various CMIP6 simulations (-0.01 to -0.03 Wm^{-2}). Following the burdens, the largest increase
683 in the 2030-2050 mean OA RF_{ARI} is calculated for the SSP3-7.0 (-0.03 Wm^{-2}), and the lowest
684 for SSP1-2.6 and 3-7.0-lowNTCF (-0.01 Wm^{-2}).

685

686 *3.2.3. Sulfate*
687 Regarding SO_4^{2-} burdens, all simulations show a statistically significant negative trend both
688 in 1990-2014 and in 2015-2050, as seen in Figure 6 and Table 5. Both the nudged AMIP-type
689 and coupled Eclipse simulations showed a 1990-2010 mean SO_4^{2-} burden of 93 kTon, while
690 the AMIP-type simulation showed a slightly larger SO_4^{2-} burden of 95 kTon, attributed to the
691 larger cloud fraction simulated in this model version (Table 2). For the 2015-2050 period, the
692 Eclipse ensemble simulates a mean Arctic SO_4^{2-} burden decrease of 30-40 kTon (32-42%),
693 compared to the 1990-2010 mean, while CMIP6 ensemble simulates a reduction of 16-45
694 kTon (16-45%). The SSP2-4.5 and Eclipse CLE scenarios simulate a very similar decrease
695 (30 kTon) in 2030-2050 mean Arctic SO_4^{2-} burdens, while the MFR and SSP1-2.6 scenarios
696 also simulate comparable reductions in the burdens (Table 5). Following the emission
697 projections, the SSP1-2.6 scenario gives the largest decrease (45 kTon: 45%), and the SSP3-
698 7.0 scenario gives the smallest reduction (16 kTons: 16%) in Arctic 2030-2050 mean SO_4^{2-}
699 burdens.

700

701   The SO_4^{2-} RF_{ARI} is decreasing (Figure 6) following the decreasing emissions (Figure 1) and
702   burdens (Figure 5). Both Eclipse and CMIP6 ensembles simulate a decrease in SO_4^{2-} RF_{ARI}
703   by 0.06-0.18 Wm^{-2}. The 2030-2050 mean SO_4^{2-} RF_{ARI} follows the burdens (Table 6), with
704   CLE and SSP2-4.5 giving similar decreases in the negative SO_4^{2-} RF_{ARI} of 0.11 Wm^{2-}, while
705   the Eclipse MFR and SSP1-2.6 simulates a very similar decrease in the 2030-2050 mean
706   SO_4^{2-} RF_{ARI} (0.16 and 0.18 Wm^{-2}, respectively).
707
708   *3.2.4. Net aerosol radiative forcing*
709   The coupled simulations in both Eclipse and CMIP6 ensemble show an Arctic RF_{ARI} of -0.32
710   to -0.35 Wm^{-2} for the 1990-2010 mean, slightly lower than recent estimates (e.g. -0.4 W m^{-2}
711   by Markowicz et al., 2021). In the Eclipse ensemble, -0.22±0.01 Wm^{-2} is calculated to be
712   originated by the anthropogenic aerosols, while in the CMIP6 near-past simulations show a
713   contribution of -019 to -0.26 Wm^{-2} from anthropogenic aerosols (Table 6b). The AMIP-type
714   Eclipse simulations calculated a much larger RF_{ARI} of -0.47 W m^{-2} for the same period,
715   which can be mainly due to the increase in the positive forcing of the BC aerosols in the
716   coupled simulations due to larger burdens. This effect is amplified due to the larger sea-ice
717   concentration simulated with the coupled model, leading to brighter surfaces compared to the
718   AMIP simulations. For the 2030-2050 period, the Eclipse ensemble simulated an increase in
719   the negative in RF_{ARI} by -0.07 W m^{-2}, while the negative anthropogenic in RF_{ARI} increased
720   by only -0.02 W m^{-2}, suggesting that the contribution from natural aerosols become more
721   important in the future. The results show that the positive dust forcing is decreased by 0.03
722   Wm^{-2} (from 0.12 Wm^{-2} to 0.09 Wm^{-2}), while the negative sea-salt forcing becomes more
723   negative by -0.03 Wm^{-2} due to the increase of ice-free ocean fraction due to melting of sea-
724   ice (see Section 3.3). For the same period, the CMIP6 future ensemble simulated an increase
725   of the negative RF_{ARI} by -0.01 Wm^{-2} to -0.06 Wm^{-2}, the largest change being in SSP1-2.6 and
726   SSP2-4.5, mainly driven by the change in BC forcing (Table 6a). Table 6 also shows that the
727   SSP1-1.6 simulates no change in the anthropogenic forcing, while SSP2-4.5 shows a similar
728   increase of -0.01 Wm^{-2} in the Eclipse ensemble. In contrary, the SSP3-7.0 and SSP3-7.0-
729   lowNTCF simulates a large decrease in the anthropogenic negative RF_{ARI} by 0.05 Wm^{-2} and
730   0.02 Wm^{-2}, respectively.
731
732   The different behavior in the two ensembles is further investigated by looking at the aerosol-
733   radiation forcing calculated for the individual aerosol species of BC, OA, SO_4^{2-} and NO_3^-
734   presented in Figure 8 that shows the box-whisker plots using the full range of scenarios. The
735   increase in cooling effect of aerosols calculated by the Eclipse ensemble is attributed mainly
736   to the decrease in BC as opposed to other aerosol species (Figure 8). More negative forcing is
737   calculated for the OA and NO_3^-, while the SO_4^{2-} forcing is becoming less negative due to
738   large reductions in SO_2 emissions (Figure 1). The net aerosol forcing is therefore slightly
739   more negative. In the CMIP6 ensemble, the BC forcing does not change as much compared
740   to the Eclipse ensemble to counteract the change in impact from SO_4^{2-}, giving a slightly more
741   positive net aerosol forcing. The CMIP6 ensemble also simulates a larger increase in the
742   negative NO_3^- forcing compared to the Eclipse ensemble (Shindell et al., 2013). Overall, the
743   changes in the different aerosol species leads to a more negative aerosol forcing by mid-
744   century (2030-2050) compared to the 1990-2010 period.

745

746 The spatial distributions of the statistically significant change in the Arctic RF_{ARI} in 2030-
747 2050 mean with respect to the 1990-2010 mean in the different ensemble members are
748 presented in Figure 9. Results show a decrease of the negative RF_{ARI} over Europe, and partly
749 over North America, and an increase over northern Pacific in all ensemble members.
750 Globally, larger changes are simulated over the East and South Asia (Figure S2), where
751 largest anthropogenic emission reductions take place. The global net RF_{ARI} is dominated by
752 the sea-salt particles, accounting for about 60% of the 1990-2010 mean forcing of -2 to -2.3
753 Wm^{-2} in and 2030-2050 mean forcing of -19 to 2.1 Wm^{-2}.
754

755 3.3. Climate change
756

757 *3.3.1. Surface air and sea surface temperatures*
758 The surface air temperature and sea-ice extent are calculated in the different simulations for
759 the 1990-2050 period. As seen in Figure 10, the Arctic surface air temperatures increase in all
760 scenarios. Between 1990 and 2014, the surface air temperatures over the Arctic increased
761 statistically significant by 0.5 °C decade^{-1} (Eclipse_CplHist) to 1 °C decade^{-1}
762 (CMIP6_Cpl_Hist), with CMIP6 showing larger increases compared to the Eclipse ensemble
763 (Table 7) . On the other hand, the observed surface air temperature during 1990-2014 shows a
764 smaller and statistically non-significant increase of 0.2 °C decade^{-1}. From 2015 onwards,
765 surface air temperatures continue to increase significantly by 0.3 to 0.6 °C decade^{-1}, with
766 larger increases in the Eclipse ensemble, due to larger reductions in the emissions and
767 therefore in the burdens and associated RF_{ARI}.
768

769 The 2030-2050 mean surface air temperatures are projected to increase by 2.1 °C and 2.3 °C
770 compared to the 1990-2010 mean temperature (Table 8, Figure 10) according to the Eclipse
771 CLE and MFR ensembles, respectively, while the CMIP6 simulation calculated an increase
772 of 1.9 °C (SSP1-2.6) to 2.2 °C (SSP3-7.0). Changes in both ensembles are statistically
773 significant on a 95% level. These warmings are smaller compared to the 4.5 - 5 °C warmer
774 2040 temperatures compared to the 1950-1980 average in the CMIP6 SSP1-2.6, SSP2-4.5
775 and SSP3-7.0 scenarios, reported by Davy and Outen (2020). It should however be noted that
776 due to the different baselines used in the present study (1990-2010) and the 1950-1980
777 baseline used in Davy and Outen (2020), it is not possible to directly compare these datasets.
778 Figure 11 shows the spatial distributions of the statistically significant (as calculated by
779 student t-test) Arctic surface air temperature change between the 1990-2010 mean and the
780 2030-2050 mean for the individual Eclipse and CMIP6 future scenarios. All scenarios
781 calculate a warming in the surface air temperatures over the central Arctic, while there are
782 differences over the land areas. The Eclipse CLE and MFR ensembles show similar warming
783 mainly over the Arctic ocean as well as North America and North East Asia and cooling over
784 the Greenland Sea. The latter is a well-known feature of observations and future projections,
785 linked, i.e., to the deep mixed layer in the area and declines in the Atlantic Meridional
786 Circulation (e.g. IPCC, 2014; Menary and Wood, 2018; Keil et al., 2020). There are also
787 differences between the Eclipse and the CMIP6 ensembles as seen in Figure 11. All CMIP6
788 scenarios show a warming over the central Arctic and a limited cooling over northern

789 Scandinavia, following the changes in RF_{ARI} shown in Figure 9, except for the SSP3-7.0
790 scenario that shows no cooling in the region. The SSP3-7.0-lowNTCF scenario shows an
791 additional cooling over Siberia. These warmings are comparable with earlier studies, such as
792 Samset et al. (2017) estimating a warming of 2.8 °C, attributed to aerosols.
793
794 *3.3.2. Sea-ice*
795 The Arctic sea-ice extent is found to decrease significantly in all simulations (Figure 10 and
796 Table 7). Similar to the near-surface temperatures, during the 1990-2014 period, the CMIP6
797 ensemble simulated a large decrease of sea-ice extent compared to the Eclipse ensemble. On
798 the other hand, the CMIP6_Cpl_Hist largely overestimated the observed decrease of 30 000
799 km^2 yr^{-1}. This overestimation has also been reported for some of the CMIP5 and CMIP6
800 models (Davy and Outten, 2020). After 2015, the Eclipse CLE ensemble projected larger
801 decreases in the sea-ice extent compared to the CMIP6 ensemble (Table 7), in agreement
802 with the changes in the near-surface temperatures. The evolutions of March and September
803 sea-ice extents, representing the Arctic annual maximum and minimum extents, respectively,
804 are also analyzed. The Eclipse ensemble projects a decrease of 23 000 ± 11 000 km^2 yr^{-1} in
805 March sea-ice extent during the 2015-2050 period, while the CMIP6 ensemble projects a
806 decrease of 10 000 ± 6000 km^2 yr^{-1} for the same period, both statistically significant. In
807 September, much larger decreases are projected by both ensembles. The Eclipse ensemble
808 simulates a decrease of 64 000 ± 10 000 km^2 yr^{-1} in the 2015-2050 period while the CMIP6
809 ensemble predicts a decrease of 50 000 ± 20 000 km^2 yr^{-1}.
810
811 The 2030-2050 annual mean sea-ice extent (Table 8) is projected to be 1.5 and 1.7 million
812 km^2 lower compared to the 1990-2010 mean in the Eclipse CLE and MFR scenarios,
813 respectively, both statistically significant on a 95% level. The CMIP6 simulations predict a
814 lower decrease of sea-ice extent by 1.2 - 1.5 million km^2, however these changes are not
815 statistically significant. These results are comparable with the results from the CMIP6 models
816 (Davy and Outten, 2020). In the 2030-2050 March mean the sea-ice extent is projected to be
817 925 000 km^2 lower in the Eclipse ensemble (statistically significant), while the CMIP6
818 ensemble projects a decrease of 991 000 km^2 (not statistically significant) A much larger
819 decrease is projected for the 2030-2050 September mean, being 2.6 million km^2 and 2.3
820 million km^2 in Eclipse and CMIP6 ensembles, respectively. As seen in Figure 12, the Eclipse
821 ensemble predicts an up to 90% lower September sea-ice fraction in a band marking the
822 maximum retreat of the sea ice line at the end of the summer, while the changes simulated by
823 the CMIP6 ensemble are not statistically significant on 95% level (therefore not shown in
824 Figure 11), which can be attributed to the single ensemble member per scenario in the CMIP6
825 ensemble, as well as the not significant changes in the near-surface temperatures (not shown).
826 In March (Figure S3), the Eclipse ensemble simulated a decrease in maximum sea-ice extent
827 at the end of winter over the northern Pacific, while the CMIP6 ensemble did not show any
828 statistically significant changes in sea-ice. In addition, the Eclipse ensemble shows a decrease
829 over the north Atlantic close to Greenland. All simulations show a similar and statistically
830 significant decrease in annual mean sea-ice extent (Figure S4 over the central Arctic, with the
831 CMIP6 ensemble showing also some increase in the sea-ice extent over the Canadian Arctic,
832 that is largest in SSP3-7.0.

833
834 The retreat in sea-ice extent also led to an increase of oceanic emissions of DMS and sea-salt
835 (Figure S5); however, the increases are not significant on a 95% significance level. The
836 simulated increase, in particular for the DMS emissions, is slightly larger in the Eclipse
837 ensemble compared to the CMIP6 ensemble, due to a larger decrease of sea-ice extent in the
838 Eclipse ensemble. Also note that GISS-E2.1 is using prescribed and fixed maps of DMS
839 concentration in the ocean. When ocean locations that are year-round under sea-ice at present
840 get exposed, the DMS that would exist in that sea water is not included in the simulations,
841 likely underestimating the increased flux of DMS into the atmosphere as the sea ice retreats.
842
843 4. Summary and Conclusions
844
845 The GISS-E2.1 earth system model has been used to simulate the recent past (1990-2014)
846 and future (2015-2050) aerosol burdens and their climate impacts over the Arctic. An
847 ensemble of seventeen simulations has been conducted, using historical and future
848 anthropogenic emissions and projections from CMIP6 and ECLIPSE V6b, the latter
849 supporting the ongoing Arctic Monitoring and Assessment Programme.
850
851 The evaluation of the recent past simulations shows underestimates of Arctic surface aerosol
852 levels by up to 50%, with the smallest biases calculated for the simulations where winds are
853 nudged, and sea-surface temperature and sea-ice are prescribed (AMIP-type: atmosphere-
854 only). An exception is SO_4^{2-}, where the nudged Eclipse AMIP simulation had the highest
855 bias, due to the high cloud bias that leads to more in-cloud sulfate production from SO_2. The
856 model skill analyses indicate slightly better performance of the CMIP6 version of the GISS-
857 E2.1 model in simulating both the aerosol levels and climate parameters compared to the
858 Eclipse version. In addition, the underestimations in the cloud properties, such as the cloud
859 fraction and liquid water path, suggest missing sources of aerosols, in particular the marine
860 sources, which can be important sources of CCN in the Arctic. Results also suggest that the
861 underestimation of both absorbing and scattering aerosol levels can partly cancel out their
862 impacts on RF_{ARI} and near-surface temperatures as the temperatures are very well reproduced
863 by the model.
864
865 From 2015 onwards, all simulations, except for the worst case CMIP6 scenario SSP3-7.0,
866 show a statistically significant decrease in the Arctic BC, OA and SO_4^{2-} burdens, with the
867 CMIP6 ensemble simulating larger aerosol burdens Eclipse, while the Eclipse ensemble
868 shows larger reductions (10-60%) in Arctic aerosol burdens compared to the reduction
869 simulated by the CMIP6 ensemble (10-45%). The largest burden reductions are calculated by
870 the highly ambitious emission reductions in the two ensembles; i.e. the Eclipse MFR (25-
871 60%) and the CMIP6 SSP1-2.6 (25-45%).
872
873 The present-day (1990-2010 mean) CMIP6 and Eclipse simulations calculated an aerosol
874 radiative forcing due to aerosol-radiation interactions (RF_{ARI}) of -0.32 to -0.35 W m^{-2}. For
875 the same period, the atmosphere only (AMIP) Eclipse simulations calculated a much larger
876 negative RF_{ARI} of -0.47 W m^{-2}. This smaller RF_{ARI} by the coupled simulations is mainly due

877   to larger BC burdens in the coupled simulations, leading to more positive forcing, which is
878   amplified by the larger albedo effect due to larger sea-ice extent simulated in the coupled
879   simulations. In the 2030-2050 period, the Eclipse ensemble simulated a RF_{ARI} -0.39±0.01 W
880   m^{-2}, of which -0.24±0.01 W m^{-2} are attributed to the anthropogenic aerosols (BC, OA, SO_4^{2-}
881   and NO_3^-). For the same period, the worst case CMIP6 scenario (SSP3-7.0) simulated a
882   similar RF_{ARI} (-0.35 W m^{-2}) compared to the 1990-2010 mean , while large emission
883   reductions led to a more negative RF_{ARI} (-0.40 W m^{-2}), mainly due to decrease in the positive
884   forcing of the BC aerosols. Overall, the Eclipse ensemble simulated slightly larger changes in
885   the RF_{ARI} over the 2015-2050 period, relative to the 1990-2010 mean, compared to the
886   CMIP6 ensemble, which can be attributed to the larger reductions in burdens in the Eclipse
887   ensemble. The differences between the two ensembles are further attributed to differences in
888   the BC and SO_4^{2-} forcings. The results suggest that the different anthropogenic emission
889   projections lead to only small differences in how the RF_{ARI} will evolve in the future over the
890   Arctic.
891
892   The future scenarios with the largest aerosol reductions, i.e. MFR in the Eclipse and SSP1-
893   2.6 in the CMIP6 ensemble projects a largest warming and sea-ice retreat. The Eclipse
894   ensemble shows a slightly larger warming of 2030-2050 mean surface air temperatures
895   compared to the 1990-2010 mean warming (2.1 to 2.5 °C) compared to that from the CMIP6
896   ensemble (1.9 °C to 2-2 °C). Larger warming in the Eclipse ensemble also resulted in a
897   slightly larger reduction in sea-ice extent (-1.5 to -1.7 million km^{-2} in CLE and MFR,
898   respectively) in 2030-2050 mean compared to the reduction in the CMIP6 scenario (-1.3 to -
899   1.6 million km^{-2} in SSP1.2-6 and SSP3-7.0, respectively). However, the changes simulated
900   by the two ensembles are within one standard deviation of each other.
901
902   The overall results showed that the aerosol burdens will substantially decrease in the short- to
903   mid-term future, implying improvements in impacts on human health and ecosystems.
904   However, the impacts of aerosols on the radiative forcing can be amplified by the sea-ice
905   extent. Results also show that even the scenarios with largest emission reductions, i.e. Eclipse
906   MFR and CMIP6 SSP1-2.6, lead to similar impact on the future Arctic surface air
907   temperatures and sea-ice loss compared to scenarios with very little mitigation such as the
908   CMIP6 SSP3-7.0, exacerbating the dominant role played by well-mixed greenhouse gases
909   and underlining the importance of continued greenhouse gas reductions.
910
911   *Author contributions.* UI coordinated the study, conducted the model simulations, as well as
912   model evaluation and analyses of the simulations, and wrote the manuscript. KT and GF
913   supported the model simulations and processing of the Eclipse V6b emissions for the GISS-
914   E2.1 model. JPF contributed to the plotting of the spatial distributions by further developing
915   the autoimage R package (French, 2017). RM prepared and provided the AOD
916   measurements, as well as the surface air temperature, sea surface temperature and sea-ice
917   data. MAT prepared the cloud observation data. CHW prepared the Arctic surface aerosol
918   measurement data. KvS coordinated the experimental setup for the Eclipse simulations in the
919   framework of the ongoing AMAP assessment. ZG prepared and provided the Eclipse V6b
920   anthropogenic emissions. HS and DCT prepared the Villum Research Station aerosol data. JB

921 and PL contributed to analyses of aerosols and climate parameters, respectively, and
922 manuscript writing. All authors contributed to the analyses and interpretation of the results, as
923 well as contributing to the writing of the manuscript.

924 *Competing Interests.* The authors declare that they have no conflict of interest.

925 *Special issue statement.* This article is part of the special issue "Arctic climate, air quality,
926 and health impacts from short-lived climate forcers (SLCFs): contributions from the AMAP
927 Expert Group".

928 *Acknowledgements.* This paper was developed as part of the Arctic Monitoring Assessment
929 Programme (AMAP), AMAP 2021Assessment: Arctic climate, air quality, and health
930 impacts from short-lived climate forcers (SLCFs). HadISST data were obtained from
931 https://www.metoffice.gov.uk/hadobs/hadisst/ and are © British Crown Copyright, Met
932 Office, provided under a Non-Commercial Government Licence
933 http://www.nationalarchives.gov.uk/doc/non-commercial-government-licence/version/2/.
934 UDel_AirT_Precip data provided by the NOAA/OAR/ESRL PSL, Boulder, Colorado, USA,
935 from their Web site at https://psl.noaa.gov/. Alert sulfate data are from Sangeeta and EC &
936 OA data from Lin Huang, respectively, as part of Canadian Aerosol Baseline Measurement
937 (CABM) program at ECCC and would like to thank operators & technicians for collection of
938 filters, calibration and analysis and Canadian Forces Services Alert for the operation of the
939 military base. These datasets are also available on Global Atmospheric Watch program,
940 World Data Center for aerosols, EBAS database (http://ebas.nilu.no/default.aspx).Aside from
941 Alert, Canada's surface air quality data are from the National Atmospheric Pollutant
942 Surveillance network (NAPS: https://open.canada.ca/data/en/dataset/1b36a356-defd-4813-
943 acea-47bc3abd859b).
944
945 Fairbanks aerosol measurements are from William Simpson and KC Nattinger. Aside from
946 Fairbanks, Alaskan measurements are from the IMPROVE network. IMPROVE is a
947 collaborative association of state, tribal, and federal agencies, and international partners. The
948 US Environmental Protection Agency is the primary funding source, with contracting and
949 research support from the National Park Service. The Air Quality Group at the University of
950 California, Davis is the central analytical laboratory, with ion analysis provided by Research
951 Triangle Institute, and carbon analysis provided by Desert Research Institute.
952 European measurements are from the EMEP network, and obtained from the EBAS database
953 (http://ebas.nilu.no). Other European data include the Gruvebadet measurements, for which
954 we acknowledge Mauro Mazzola (mauro.mazzola@cnr.it), Stefania Gilardoni
955 (stefania.gilardoni@cnr.it), and Angelo Lupi (angelo.lupi@cnr.it) from the Institute of Polar
956 Sciences fo Gruvabadet eBC measurements; and Rita Traversi (rita.traversi@unifi.it), Mirko
957 Severi (mirko.severi@unifi.it), and Silvia Becagli (silvia.becagli@unifi.it) from University
958 of Florence http://www.isac.cnr.it/~radiclim/CCTower/ ?Data:Aerosol; the Zeppelin datasets,
959 for which we acknowledge Vito Vitale and Angelo Lupi (also available on
960 http://ebas.nilu.no); and the Villum Station datasets (www.villumresearchstation.dk) from
961 Henrik Skov (hsk@envs.au.dk; also available in http://ebas.nilo.no). The AERONET AOD

measurements were obtained from NASA's Goddard Space Flight Center
(https://aeronet.gsfc.nasa.gov/new_web/index.html). The authors acknowledge Dr. L.
Sogacheva and AEROSAT team for satellite based merged AOD data.

Financial support. This research has been supported by the Aarhus University
Interdisciplinary Centre for Climate Change (iClimate) OH fund (no. 2020-0162731), the
FREYA project, funded by the Nordic Council of Ministers (grant agreement no. MST-227-
00036 and MFVM-2019-13476), and the EVAM-SLCF funded by the Danish Environmental
Agency (grant agreement no. MST-112-00298). KT and GF thank the NASA Modeling,
Analysis and Prediction program (MAP) for support. ZK was financially supported by the
EU-funded Action on Black Carbon in the Arctic (EUA-BCA) under the EU Partnership
Instrument. JPF was partially supported by NSF award 1915277.

References

Abbatt, J. P. D., Leaitch, W. R., Aliabadi, A. A., Bertram, A. K., Blanchet, J.-P., Boivin-
Rioux, A., Bozem, H., Burkart, J., Chang, R. Y. W., Charette, J., Chaubey, J. P., Christensen,
R. J., Cirisan, A., Collins, D. B., Croft, B., Dionne, J., Evans, G. J., Fletcher, C. G., Galí, M.,
Ghahremaninezhad, R., Girard, E., Gong, W., Gosselin, M., Gourdal, M., Hanna, S. J.,
Hayashida, H., Herber, A. B., Hesaraki, S., Hoor, P., Huang, L., Hussherr, R., Irish, V. E.,
Keita, S. A., Kodros, J. K., Köllner, F., Kolonjari, F., Kunkel, D., Ladino, L. A., Law, K.,
Levasseur, M., Libois, Q., Liggio, J., Lizotte, M., Macdonald, K. M., Mahmood, R., Martin,
R. V., Mason, R. H., Miller, L. A., Moravek, A., Mortenson, E., Mungall, E. L., Murphy, J.
G., Namazi, M., Norman, A.-L., O'Neill, N. T., Pierce, J. R., Russell, L. M., Schneider, J.,
Schulz, H., Sharma, S., Si, M., Staebler, R. M., Steiner, N. S., Thomas, J. L., von Salzen, K.,
Wentzell, J. J. B., Willis, M. D., Wentworth, G. R., Xu, J.-W., and Yakobi-Hancock, J. D.:
Overview paper: New insights into aerosol and climate in the Arctic, Atmos. Chem. Phys.,
19, 2527–2560, https://doi.org/10.5194/acp-19-2527-2019, 2019.

AMAP 2021 Assessment: Arctic climate, air quality, and health impacts from short-lived
climate forcers (SLCFs).

AMAP, 2015. AMAP Assessment 2015: Black carbon and ozone as Arctic climate forcers.
Arctic Monitoring and Assessment Programme (AMAP), Oslo, Norway. vii + 116 pp.

Amann, M., Bertok, I., Borken-Kleefeld, J., Cofala, J., Heyes, C., Höglund-Isaksson, L.,
Klimont, Z., Nguyen, B., Posch, M., Rafaj, P., Sandler, R., Schöpp, W., Wagner, F.,
Winiwarter, W.: Cost-effective control of air quality and greenhouse gases in Europe:
Modeling and policy applications. Environmental Modelling & Software, 26, (12), 1489-
1501, 2011.

Ångström, A.: On the Atmospheric Transmission of Sun Radiation and on Dust in the Air.
Geografiska Annaler, 11, 156-166. doi:10.2307/519399, 1929.

1002 Bauer, S. E., Tsigaridis, K., Faluvegi, G.,Kelley, M., Lo, K. K., & Miller, R. L.,et al.:
1003 Historical (1850–2014) aerosol evolution and role on climate forcing using the GISS
1004 ModelE2.1contribution to CMIP6. Journal ofAdvances in Modeling Earth Systems,12,
1005 e2019MS001978, https://doi.org/10.1029/2019MS001978, 2020.

1006 Bauer, S.E., and Koch, D.: Impact of heterogeneous sulfate formation at mineral dust
1007 surfaces on aerosol loads and radiative forcing in the Goddard Institute for Space Studies
1008 general circulation model. J. Geophys. Res., 110, D17202, doi:10.1029/2005JD005870, 2005.

1009 Bond, T.C., Doherty, S.J., Fahey, D.W., Forster, P.M. , Berntsen, T., De Angelo, B.J.,
1010 Flanner, M.G., Ghan, S., Karcher, B., Koch, D., Kinne, S., Kondo, Y., Quiinn, P.K., Sarofim,
1011 M.C., Schultz, M.G., Schulz, M., Venkataraman, C., Zhang, H., Zhang, S., Bellouin, N.,
1012 Guttikunda, S.K., Hopke, P.K., Jacobson, M.Z., Kaiser, J.W., Klimont, Z., Lohmann, U.,
1013 Schwarz, J.P., Shindell, D., Storelvmo, T., Warren, S.G., Zender, C.S.: Bounding the role of
1014 black carbon in the climate system: a scientific assessment, J. Geophys. Res. Atmos., 118
1015 (11), 5380-5552, 10.1002/jgrd.50171, 2013.

1016 Bond, T. C., D. G. Streets, K. F. Yarber, S. M. Nelson, J. H. Woo, and Z. Klimont: A
1017 technology-based global inventory of black and organic carbon emissions from combustion,
1018 J. Geophys. Res., 109, D14203, doi:10.1029/2003JD003697, 2014.

1019 Boy, M., Thomson, E. S., Acosta Navarro, J.-C., Arnalds, O., Batchvarova, E., Bäck, J.,
1020 Berninger, F., Bilde, M., Brasseur, Z., Dagsson-Waldhauserova, P., Castarède, D., Dalirian,
1021 M., de Leeuw, G., Dragosics, M., Duplissy, E.-M., Duplissy, J., Ekman, A. M. L., Fang, K.,
1022 Gallet, J.-C., Glasius, M., Gryning, S.-E., Grythe, H., Hansson, H.-C., Hansson, M., Isaksson,
1023 E., Iversen, T., Jonsdottir, I., Kasurinen, V., Kirkevåg, A., Korhola, A., Krejci, R.,
1024 Kristjansson, J. E., Lappalainen, H. K., Lauri, A., Leppäranta, M., Lihavainen, H.,
1025 Makkonen, R., Massling, A., Meinander, O., Nilsson, E. D., Olafsson, H., Pettersson, J. B.
1026 C., Prisle, N. L., Riipinen, I., Roldin, P., Ruppel, M., Salter, M., Sand, M., Seland, Ø., Seppä,
1027 H., Skov, H., Soares, J., Stohl, A., Ström, J., Svensson, J., Swietlicki, E., Tabakova, K.,
1028 Thorsteinsson, T., Virkkula, A., Weyhenmeyer, G. A., Wu, Y., Zieger, P., and Kulmala, M.:
1029 Interactions between the atmosphere, cryosphere, and ecosystems at northern high latitudes,
1030 Atmos. Chem. Phys., 19, 2015–2061, https://doi.org/10.5194/acp-19-2015-2019, 2019.

1031 Breider, T. J., Mickley, L. J., Jacob, D. J., Ge, C., Wang, J., Payer Sulprizio, M., Croft, B.,
1032 Ridley, D. A., McConnell, J. R., Sharma, S., Husain, L., Dutkiewicz, V. A., Eleftheriadis, K.,
1033 Skov, H. and Hopke, P. K.: Multidecadal trends in aerosol radiative forcing over the Arctic:
1034 Contribution of changes in anthropogenic aerosol to Arctic warming since 1980, J. Geophys.
1035 Res. Atmos., 122(6), 3573–3594, doi:10.1002/2016JD025321, 2017.

1036 Burnett, R., Chena, H., Szyszkowicza, M., Fann, N., Hubbell, B., Pope III, C. A., Apte, J. S.,
1037 Brauer, M., Cohen, A., Weichenthal, S., Coggins, J., Di Q., Brunekreef B., Frostad, J., Lim,
1038 S. S., Kan, H., Walker, K. D., Thurston, G. D., Hayes, R. B., Lim, C. C., Turner, M. C.,
1039 Jerrett, M., Krewski, D., Gapstur, S. M., Diver, W. R., Ostro, B., Goldberg, D., Crouse, D.
1040 L., Martin, R. V., Peters, P., Pinault, L., Tjepkema, M., van Donkelaar, M., Villeneuve, P. J.,
1041 Miller, A. B., Yin, P., Zhou, M., Wang, L., Janssen, N. A. H., Marra, M., Atkinson, R. W.,
1042 Tsang, H., Thach, T. Q., Cannon, J. B., Allen, R. T., Hart, J. E., Laden, F., Cesaroni, G.,

1043 Forastiere, F., Weinmayr, G., Jaensch, A., Nagel, G., Concin, H. and Spadar, J. V., Global
1044 estimates of mortality associated with long term exposure to outdoor fine particulate matter.
1045 Proceedings of the National Academy of Sciences, 38 (115), pp. 9592–9597. doi:
1046 10.1073/pnas.1803222115. 2018.

1047 Clarke, A.D., and Noone, K.J.: Soot in the Arctic snowpack: A cause for perturbations in
1048 radiative transfer, Atmos. Environ., 19, 2045– 2053, 1985.

1049 Collins, W. J., Lamarque, J.-F., Schulz, M., Boucher, O., Eyring, V., Hegglin, M. I.,
1050 Maycock, A., Myhre, G., Prather, M., Shindell, D., and Smith, S. J.: AerChemMIP:
1051 quantifying the effects of chemistry and aerosols in CMIP6, Geosci. Model Dev., 10, 585–
1052 607, https://doi.org/10.5194/gmd-10-585-2017, 2017.

1053 Davy, R., and Outten, S.: The Arctic Surface Climate in CMIP6: Status and Developments
1054 since CMIP5, *J. Climate*, 33 (18), 8047–8068, https://doi.org/10.1175/JCLI-D-19-0990.1,
1055 2020.

1056 Dumont, M., Brun, E., Picard, G. et al.: Contribution of light-absorbing impurities in snow to
1057 Greenland's darkening since 2009. Nature Geosci 7, 509–512,
1058 https://doi.org/10.1038/ngeo2180, 2014.

1059 Eck, T.F., B.N.Holben, J.S.Reid, O.Dubovik, A.Smirnov, N.T.O'Neill, I.Slutsker, and
1060 S.Kinne: Wavelength dependence of the optical depth of biomass burning, urban and desert
1061 dust aerosols, J. Geophys. Res., 104, 31 333-31 350, 1999.

1062 Eckhardt, S., Quennehen, B., Olivié, D. J. L., Berntsen, T. K., Cherian, R., Christensen, J. H.,
1063 Collins, W., Crepinsek, S., Daskalakis, N., Flanner, M., Herber, A., Heyes, C., Hodnebrog,
1064 Ø., Huang, L., Kanakidou, M., Klimont, Z., Langner, J., Law, K. S., Lund, M. T., Mahmood,
1065 R., Massling, A., Myriokefalitakis, S., Nielsen, I. E., Nøjgaard, J. K., Quaas, J., Quinn, P. K.,
1066 Raut, J.-C., Rumbold, S. T., Schulz, M., Sharma, S., Skeie, R. B., Skov, H., Uttal, T., von
1067 Salzen, K., and Stohl, A.: Current model capabilities for simulating black carbon and sulfate
1068 concentrations in the Arctic atmosphere: a multi-model evaluation using a comprehensive
1069 measurement data set, Atmos. Chem. Phys., 15, 9413–9433, https://doi.org/10.5194/acp-15-
1070 9413-2015, 2015.

1071 Eyring, V., Bony, S., Meehl, G. A., Senior, C. A., Stevens, B., Stouffer, R. J., and Taylor, K.
1072 E.: Overview of the Coupled Model Intercomparison Project Phase 6 (CMIP6) experimental
1073 design and organization, Geosci. Model Dev., 9, 1937–1958, https://doi.org/10.5194/gmd-9-
1074 1937-2016, 2016.

1075 Feng, L., Smith, S. J., Braun, C., Crippa, M., Gidden, M. J., Hoesly, R., Klimont, Z., van
1076 Marle, M., van den Berg, M., and van der Werf, G. R.: The generation of gridded emissions
1077 data for CMIP6, Geosci. Model Dev., 13, 461–482, https://doi.org/10.5194/gmd-13-461-
1078 2020, 2020.

1079 Flanner, M.G., Zender, C.S., Randerson, J.T., and Rasch, P.J.: Present-day climate forcing
1080 and response from blackcarbon in snow, J. Geophys. Res., 112, D11202,
1081 doi:10.1029/2006JD008003, 2007.

1082 French, J.P.: autoimage: Multiple Heat Maps for Projected Coordinates, The R Journal, 9
1083 (1), 284-297, 2017.

1084 Gagné, M.-È., Gillett, N.P., and Fyfe, J. C.: Impact of aerosolemission controls on
1085 futureArctic sea ice cover, Geo-phys. Res. Lett., 42, 8481–8488,doi:10.1002/2015GL065504,
1086 2015.

1087 Gery, M., Whitten, G.Z., Killus, J.P., and Dodge, M.C.: A photochemical kinetics mechanism
1088 for urban and regional scale computer modelling, J.Geophys.Res., 94, 18925-18956, 1989.

1089 Gidden, M. J., Riahi, K., Smith, S. J., Fujimori, S., Luderer, G., Kriegler, E., van Vuuren, D.
1090 P., van den Berg, M., Feng, L., Klein, D., Calvin, K., Doelman, J. C., Frank, S., Fricko, O.,
1091 Harmsen, M., Hasegawa, T., Havlik, P., Hilaire, J., Hoesly, R., Horing, J., Popp, A., Stehfest,
1092 E., and Takahashi, K.: Global emissions pathways under different socioeconomic scenarios
1093 for use in CMIP6: a dataset of harmonized emissions trajectories through the end of the
1094 century, Geosci. Model Dev., 12, 1443–1475, https://doi.org/10.5194/gmd-12-1443-2019,
1095 2019.

1096 Gidden, M. J., Fujimori, S., van den Berg, M., Klein, D., Smith, S. J., van Vuuren, D. P., and
1097 Riahi, K.: A methodology and implementation of automated emissions harmonization for use
1098 in Integrated Assessment Models, Environ. Modell. Softw., 105, 187–200, 2018.

1099 Graversen R, Langen P.L.: On the Role of the Atmospheric Energy Transport in 2xCO2-
1100 Induced Polar Amplification in CESM1. Journal of Climate, 32(13), 3941-3956, 2019.

1101 Gryspeerdt, E., Goren, T., Sourdeval, O., Quaas, J., Mülmenstädt, J., Dipu, S., Unglaub, C.,
1102 Gettelman, A., and Christensen, M.: Constraining the aerosol influence on cloud liquid water
1103 path, Atmos. Chem. Phys., 19, 5331–5347, https://doi.org/10.5194/acp-19-5331-2019, 2019.

1104 Hansen, J., M. Sato, R. Ruedy, L. Nazarenko, A. Lacis, G.A. Schmidt, G. Russell, I. Aleinov,
1105 M. Bauer, S. Bauer, N. Bell, B. Cairns, V. Canuto, M. Chandler, Y. Cheng, A. Del Genio, G.
1106 Faluvegi, E. Fleming, A. Friend, T. Hall, C. Jackman, M. Kelley, N.Y. Kiang, D. Koch, J.
1107 Lean, J. Lerner, K. Lo, S. Menon, R.L. Miller, P. Minnis, T. Novakov, V. Oinas, J.P.
1108 Perlwitz, J. Perlwitz, D. Rind, A. Romanou, D. Shindell, P. Stone, S. Sun, N. Tausnev, D.
1109 Thresher, B. Wielicki, T. Wong, M. Yao, and S. Zhang: Efficacy of climate forcings. J.
1110 Geophys. Res., 110, D18104, doi:10.1029/2005JD005776, 2005.

1111 Hoesly, R. M., Smith, S. J., Feng, L., Klimont, Z., Janssens-Maenhout, G., Pitkanen, T.,
1112 Seibert, J. J., Vu, L., Andres, R. J., Bolt, R. M., Bond, T. C., Dawidowski, L., Kholod, N.,
1113 Kurokawa, J.-I., Li, M., Liu, L., Lu, Z., Moura, M. C. P., O'Rourke, P. R., and Zhang, Q.:
1114 Historical (1750–2014) anthropogenic emissions of reactive gases and aerosols from the
1115 Community Emissions Data System (CEDS), Geosci. Model Dev., 11, 369–408,
1116 https://doi.org/10.5194/gmd-11-369-2018, 2018.

1117 Holben B.N., T.F.Eck, I.Slutsker, D.Tanre, J.P.Buis, A.Setzer, E.Vermote, J.A.Reagan,
1118 Y.Kaufman, T.Nakajima, F.Lavenu, I.Jankowiak, and A.Smirnov: AERONET - A federated
1119 instrument network and data archive for aerosol characterization, Rem. Sens. Environ., 66, 1-
1120 16, 1998.

1121 Höglund-Isaksson, L., Gómez-Sanabria, A., Klimont, Z., Rafaj, P., Schöpp, W.: Technical
1122 potentials and costs for reducing global anthropogenic methane emissions in the 2050
1123 timeframe –results from the GAINS model. Environmental Research Communications, 2 (2),
1124 2020.

1125 International Energy Agency (IEA): World Energy Outlook 2018, 661 pp., ISBN 978-92-64-
1126 30677-6, 2018.

1127 IPCC, 2014: Climate Change 2014: Synthesis Report. Contribution of Working Groups I, II
1128 and III to the Fifth Assessment Report of the Intergovernmental Panel on Climate Change
1129 [Core Writing Team, R.K. Pachauri and L.A. Meyer (eds.)]. IPCC, Geneva, Switzerland, 151
1130 pp.

1131 IPCC, 2013: Climate Change 2013: The Physical Science Basis. Contribution of Working
1132 Group I to the Fifth Assessment Report of the Intergovernmental Panel on Climate Change
1133 [Stocker, T.F., D. Qin, G.-K. Plattner, M. Tignor, S.K. Allen, J. Boschung, A. Nauels, Y. Xia,
1134 V. Bex and P.M. Midgley (eds.)]. Cambridge University Press, Cambridge, United Kingdom
1135 and New York, NY, USA, 1535 pp.

1136 Jacobson, M. Z.: Strong radiative heating due to the mixing state of black carbon in the
1137 atmospheric aerosols, Nature, 409, 695–698, 2001.

1138 Karlsson, K.-G., Devasthale, A: Inter-Comparison and Evaluation of the Four Longest
1139 Satellite-Derived Cloud Climate Data Records: CLARA-A2, ESA Cloud CCI V3, ISCCP-
1140 HGM, and PATMOS-x. Remote Sens. 2018, 10, 1567.

1141 Karlsson, K.-G., Anttila, K., Trentmann, J., Stengel, M., Fokke Meirink, J., Devasthale, A.,
1142 Hanschmann, T., Kothe, S., Jääskeläinen, E., Sedlar, J., Benas, N., van Zadelhoff, G.-J.,
1143 Schlundt, C., Stein, D., Finkensieper, S., Håkansson, N., and Hollmann, R.: CLARA-A2: the
1144 second edition of the CM SAF cloud and radiation data record from 34 years of global
1145 AVHRR data, Atmos. Chem. Phys., 17, 5809–5828, https://doi.org/10.5194/acp-17-5809-
1146 2017, 2017.

1147 Karlsson, Karl-Göran; Anttila, Kati; Trentmann, Jörg; Stengel, Martin; Meirink, Jan Fokke;
1148 Devasthale, Abhay; Hanschmann, Timo; Kothe, Steffen; Jääskeläinen, Emmihenna; Sedlar,
1149 Joseph; Benas, Nikos; van Zadelhoff, Gerd-Jan; Schlundt, Cornelia; Stein, Diana;
1150 Finkensieper, Stephan; Håkansson, Nina; Hollmann, Rainer; Fuchs, Petra; Werscheck,
1151 Martin (2017): CLARA-A2: CM SAF cLoud, Albedo and surface RAdiation dataset from
1152 AVHRR data - Edition 2, Satellite Application Facility on Climate Monitoring,
1153 https://doi.org/10.5676/EUM_SAF_CM/CLARA_AVHRR/V002 (last access: October 26th
1154 2020).

1155 Kay, J., and L'Ecuyer, T.: Observational constraints on Arctic Ocean clouds and radiative
1156 fluxes during the early 21st century. Journal of Geophysical Research: Atmospheres. 118.
1157 10.1002/jgrd.50489, 2013.

1158 Keil, P., Mauritsen, T., Jungclaus, J. *et al.* Multiple drivers of the North Atlantic warming
1159 hole. *Nat. Clim. Chang.* 10, 667–671, https://doi.org/10.1038/s41558-020-0819-8, 2020.

Kelley, M., Schmidt, G. A., Nazarenko, L. S., Bauer, S. E., Ruedy, R., Russell, G. L., et al.: GISS-E2.1: Configurations and climatology. Journal of Advances in Modeling Earth Systems, 12, e2019MS002025. https://doi.org/10.1029/2019MS002025, 2020.

Klimont, Heyes, Rafaj, Schoepp, Purohit, Cofala, Hoglund-Isaksson, Wagner,...et al. Global scenarios of anthropogenic emissions of air pollutants: ECLIPSE (in preparation for GMD)

Klimont, Z., Kupiainen, K., Heyes, C., Purohit, P., Cofala, J., Rafaj, P., Borken-Kleefeld, J., and Schöpp, W.: Global anthropogenic emissions of particulate matter including black carbon, Atmos. Chem. Phys., 17, 8681–8723, https://doi.org/10.5194/acp-17-8681-2017, 2017.

Lamarque, J.-F., Bond, T. C., Eyring, V., Granier, C., Heil, A., Klimont, Z., Lee, D., Liousse, C., Mieville, A., Owen, B., Schultz, M. G., Shindell, D., Smith, S. J., Stehfest, E., Van Aardenne, J., Cooper, O. R., Kainuma, M., Mahowald, N., McConnell, J. R., Naik, V., Riahi, K., and van Vuuren, D. P.: Historical (1850–2000) gridded anthropogenic and biomass burning emissions of reactive gases and aerosols: methodology and application, Atmos. Chem. Phys., 10, 7017–7039, https://doi.org/10.5194/acp-10-7017-2010, 2010.

Lelieveld, J., Klingmüller, K., Pozzer, A., Pöschl, U., Fnais, M., Daiber, A., Münzel, T. Cardiovascular disease burden from ambient air pollution in Europe reassessed using novel hazard ratio functions. European Heart Journal 40, 1590-1596. https://doi.org/10.1093/eurheartj/ehz135, 2019.

Lenssen, N. J. L., Schmidt, G. A., Hansen, J. E., Menne, M. J., Persin, A., Ruedy, R. and Zyss, D.: Improvements in the GISTEMP Uncertainty Model. Journal of Geophysical Research: Atmospheres 124: 6307-6326 10.1029/2018jd029522, 2019.

Lewinschal, A., Ekman, A. M. L., Hansson, H. C., Sand, M., Berntsen, T. K., & Langner, J. (2019). Local and remote temperature response of regional SO2 emissions. Atmospheric Chemistry and Physics, 19, 2385– 2403. https://doi.org/10.5194/acp-19-2385-2019

Lund, M. T., Myhre, G., Haslerud, A. S., Skeie, R. B., Griesfeller, J., Platt, S. M., Kumar, R., Myhre, C. L., and Schulz, M.: Concentrations and radiative forcing of anthropogenic aerosols from 1750 to 2014 simulated with the Oslo CTM3 and CEDS emission inventory, Geosci. Model Dev., 11, 4909–4931, https://doi.org/10.5194/gmd-11-4909-2018, 2018.

Lund, M. T., Berntsen, T. K., and Samset, B. H.: Sensitivity of black carbon concentrations and climate impact to aging and scavenging in OsloCTM2-M7, Atmos. Chem. Phys., 17, 6003–6022, https://doi.org/10.5194/acp-17-6003-2017, 2017.

Mahmood, R., von Salzen, K., Norman, A.-L., Galí, M., and Levasseur, M.: Sensitivity of Arctic sulfate aerosol and clouds to changes in future surface seawater dimethylsulfide concentrations, Atmos. Chem. Phys., 19, 6419–6435, https://doi.org/10.5194/acp-19-6419-2019, 2019.

Markowicz, K.M.,Lisok, J., Xian, P.: Simulation of long-term direct aerosol radiative forcing over the arctic within the framework of the iAREA project. Atmospheric Environment, 244, 117882, 2021.

1199 Menary, M.B., Wood, R.A.: An anatomy of the projected North Atlantic warming hole in
1200 CMIP5 models. *Clim Dyn* 50, 3063–3080, https://doi.org/10.1007/s00382-017-3793-8, 2018.

1201 Menon, S., and Rotstayn, L.: The radiative influence of aerosol effects on liquid-phase
1202 cumulus and stratus clouds based on sensitivity studies with two climate models, Clim. Dyn.,
1203 27, 345– 356, 2006.

1204 Miller, R.L., G.A. Schmidt, L. Nazarenko, S.E. Bauer, M. Kelley, R. Ruedy, G.L. Russell, A.
1205 Ackerman, I. Aleinov, M. Bauer, R. Bleck, V. Canuto, G. Cesana, Y. Cheng, T.L. Clune, B.
1206 Cook, C.A. Cruz, A.D. Del Genio, G.S. Elsaesser, G. Faluvegi, N.Y. Kiang, D. Kim, A.A.
1207 Lacis, A. Leboissetier, A.N. LeGrande, K.K. Lo, J. Marshall, E.E. Matthews, S. McDermid,
1208 K. Mezuman, L.T. Murray, V. Oinas, C. Orbe, C. Pérez García-Pando, J.P. Perlwitz, M.J.
1209 Puma, D. Rind, A. Romanou, D.T. Shindell, S. Sun, N. Tausnev, K. Tsigaridis, G. Tselioudis,
1210 E. Weng, J. Wu, and M.-S. Yao: CMIP6 historical simulations (1850-2014) with GISS-E2.1.
1211 J. Adv. Model. Earth Syst., in press, doi:10.1029/2019MS002034, 2020.

1212 Miller, R.L., G.A. Schmidt, and D.T. Shindell: Forced annular variations in the 20th century
1213 Intergovernmental Panel on Climate Change Fourth Assessment Report models. J. Geophys.
1214 Res., 111, D18101, doi:10.1029/2005JD006323, 2006.

1215 Myhre, G., D. Shindell, F.-M. Bréon, W. Collins, J. Fuglestvedt, J. Huang, D. Koch, J.-F.
1216 Lamarque, D. Lee, B. Mendoza, T. Nakajima, A. Robock, G. Stephens, T. Takemura, and H.
1217 Zhang: Anthropogenic and natural radiative forcing. In Climate Change 2013: The Physical
1218 Science Basis. Contribution of Working Group I to the Fifth Assessment Report of the
1219 Intergovernmental Panel on Climate Change. T.F. Stocker, D. Qin, G.-K. Plattner, M. Tignor,
1220 S.K. Allen, J. Doschung, A. Nauels, Y. Xia, V. Bex, and P.M. Midgley, Eds. Cambridge
1221 University Press, pp. 659-740, doi:10.1017/CBO9781107415324.018, 2013.

1222 Platnick, S., S. A. Ackerman, M. D. King, K. Meyer, W. P. Menzel, R. E. Holz, B. A. Baum,
1223 and P. Yang: MODIS atmosphere L2 cloud product (06_L2), NASA MODIS Adaptive
1224 Processing System, Goddard Space Flight Center, 2015.

1225 Quinn, P.K., Shaw, G., Andrews, E., Dutton, E.G., Ruoho-Airola, T., Gong, S.L. Arctic haze:
1226 current trends and knowledge gaps, Tellus B: Chemical and Physical Meteorology, 59:1, 99-
1227 114, DOI: 10.1111/j.1600-0889.2006.00236.x, 2007.

1228 Rao, S., Klimont, Z., Smith, S.J., Van Dingenen, R., Dentener, F., Bouwman, L., Riahia, K.,
1229 Amann, M., Bodirsky, B.L., van Vuuren, D.P., Reis, L.A., Calvin, K., Drouet, L., Fricko, O.,
1230 Fujimori, S., Gernaat, D., Havlik, P., Harmsen, M., Hasegawa, T., Heyes, C., Hilaire, J.,
1231 Luderer, G., Masui, T., Stehfest, E., Strefler, J., van der Slui, S., Tavonil, M.: Future air
1232 pollution in the Shared Socio-economic Pathways. Global Environmental Change, 42, 346-
1233 358, 2017.

1234 Rayner, N. A., D. E. Parker, E. B. Horton, C. K. Folland, L. V. Alexander, D. P. Rowell, E.
1235 C. Kent, and A. Kaplan, Global analyses of sea surface temperature, sea ice, and night marine
1236 air temperature since the late nineteenth century, J. Geophys. Res.,108(D14), 4407,
1237 doi:10.1029/2002JD002670, 2003.

Ren, L., Yang, Y., Wang, H., Zhang, R., Wang, P., and Liao, H.: Source attribution of Arctic black carbon and sulfate aerosols and associated Arctic surface warming during 1980–2018, Atmos. Chem. Phys., 20, 9067–9085, https://doi.org/10.5194/acp-20-9067-2020, 2020.

Reynolds, R.W., Rayner, N.A., Smith, T.M., Stokes, D.C., and Wang, W. An improved in situ and satellite SST analysis for climate. J. Climate, 15, 1609-1625, 2002.

Riahi, K.,van Vuuren, D.P., Kriegler, E., Edmonds, J., O'Neil, B.C., Fujimori, S., Bauer, N., Calvin, K., Dellink, R., Fricko, O., Lutz, W., Popp, A., Cuaresma, C.J., KC, S., Leimbach, M., Jiang, L., Kram, T., Rao, S., Emmerling, J., Ebi, K., Hasegawa, T., Havlik, P., Humpenöder, F., Da Silva, L.A:, Smith, S., Stehfest, E., Bosetti, V., Eom, J., Gernaat, D., Masui, T., Rogelj, J., Strefler, J., Drouet, L., Krey, V., Luderer, G., Harmsen, M., Takahashi, K., Baumstark, L., Doelman, J.C., Kainuma, M., Klimont, Z., Marangoni, G., Lotze-Campen, H., Obersteiner, M., Tabeau, A., Tavoni, M.: The Shared Socioeconomic Pathways and their energy, land use, and greenhouse gas emissions implications: An overview. Global Environmental Change, 42, 153-168, 2017.

Samset, B. H., Sand, M., Smith, C. J., Bauer, S. E., Forster, P. M., Fuglestvedt, J. S., Osprey, S., & Schleussner, C.-F.: Climate impacts from a removal of anthropogenic aerosol emissions. Geophysical Research Letters, 45. https://doi.org/10.1002/2017GL076079, 2018.

Sand, M., T. K. Berntsen, K. von Salzen, M. G. Flanner, J. Langner, and D. G. Victor: Response of arctic temperature to changes in emissions of short-lived climate forcers, Nat. Clim. Change, 6, 286–289, doi:10.1038/nclimate2880, 2015.

Sayer, A. M., Hsu, N. C., Lee, J., Kim, W. V., Dubovik, O., Dutcher, S. T. et al.: Validation of SOAR VIIRS over-water aerosol retrievals and context within the global satellite aerosol data record. Journal of Geophysical Research: Atmospheres, 123, 13,496–13,526, https://doi.org/10.1029/2018JD029465, 2018.

Sayer, A. M. and Knobelspiesse, K. D.: How should we aggregate data? Methods accounting for the numerical distributions, with an assessment of aerosol optical depth, Atmos. Chem. Phys., 19, 15023–15048, https://doi.org/10.5194/acp-19-15023-2019, 2019.

Schacht, J., Heinold, B., Quaas, J., Backman, J., Cherian, R., Ehrlich, A., Herber, A., Huang, W. T. K., Kondo, Y., Massling, A., Sinha, P. R., Weinzierl, B., Zanatta, M., and Tegen, I.: The importance of the representation of air pollution emissions for the modeled distribution and radiative effects of black carbon in the Arctic, Atmos. Chem. Phys., 19, 11159–11183, https://doi.org/10.5194/acp-19-11159-2019, 2019.

Schmale, J., Zieger, P., Ekman, A.M.L. Aerosols in current and future Arctic climate. Nature Climate Change, 11, 95–105, https://doi.org/10.1038/s41558-020-00969-5, 2021.

Schutgens, N. A. J.: Site representativity of AERONET and GAW remotely sensed aerosol optical thickness and absorbing aerosol optical thickness observations, Atmos. Chem. Phys., 20, 7473–7488, https://doi.org/10.5194/acp-20-7473-2020, 2020a.

Schutgens, N., Sayer, A. M., Heckel, A., Hsu, C., Jethva, H., de Leeuw, G., Leonard, P. J. T., Levy, R. C., Lipponen, A., Lyapustin, A., North, P., Popp, T., Poulson, C., Sawyer, V., Sogacheva, L., Thomas, G., Torres, O., Wang, Y., Kinne, S., Schulz, M., and Stier, P.: An

1278   AeroCom/AeroSat study: Intercomparison of Satellite AOD Datasets for Aerosol Model
1279   Evaluation, Atmos. Chem. Phys. Discuss., https://doi.org/10.5194/acp-2019-1193, in review,
1280   2020b.

1281   Semmler, T., Pithan, F., Jung, T.: Quantifying two-way influences between the Arctic and
1282   mid-latitudes through regionally increased CO2 concentrations in coupled climate
1283   simulations, *Climate Dynamics*, 54, 3307–3321, 2020.

1284   Serreze, M.C., Francis, J.A. The Arctic Amplification Debate. Climatic Change 76, 241–264,
1285   https://doi.org/10.1007/s10584-005-9017-y, 2006.

1286   Shindell, D. T., Lamarque, J.-F., Schulz, M., Flanner, M., Jiao, C., Chin, M., Young, P. J.,
1287   Lee, Y. H., Rotstayn, L., Mahowald, N., Milly, G., Faluvegi, G., Balkanski, Y., Collins, W.
1288   J., Conley, A. J., Dalsoren, S., Easter, R., Ghan, S., Horowitz, L., Liu, X., Myhre, G.,
1289   Nagashima, T., Naik, V., Rumbold, S. T., Skeie, R., Sudo, K., Szopa, S., Takemura, T.,
1290   Voulgarakis, A., Yoon, J.-H., and Lo, F.: Radiative forcing in the ACCMIP historical and
1291   future climate simulations, Atmos. Chem. Phys., 13, 2939–2974, https://doi.org/10.5194/acp-
1292   13-2939-2013, 2013.

1293   Shindell, D., J.C.I. Kuylenstierna, E. Vignati, R. van Dingenen, M. Amann, Z. Klimont, S.C.
1294   Anenberg, N. Muller, G. Janssens-Maenhout, F. Raes, J. Schwartz, G. Faluvegi, L. Pozzoli,
1295   K. Kupiainen, L. Höglund-Isaksson, L. Emberson, D. Streets, V. Ramanathan, K. Hicks,
1296   N.T.K. Oanh, G. Milly, M. Williams, V. Demkine, and D. Fowler, Simultaneously mitigating
1297   near-term climate change and improving human health and food security. Science, 335, 183-
1298   189, doi:10.1126/science.1210026, 2012.

1299   Shindell, D., and G. Faluvegi,: Climate response to regional radiative forcing during the
1300   twentieth century. Nature Geosci., 2, 294-300, doi:10.1038/ngeo473, 2009.

1301   Shindell, D.: Local and remote contributions to Arctic warming, Geophysical Research
1302   Letters – Climate, 34, L14704, https://doi.org/10.1029/2007GL030221, 2007.

1303   Sogacheva, L., Popp, T., Sayer, A. M., Dubovik, O., Garay, M. J., Heckel, A., Hsu, N. C.,
1304   Jethva, H., Kahn, R. A., Kolmonen, P., Kosmale, M., de Leeuw, G., Levy, R. C., Litvinov, P.,
1305   Lyapustin, A., North, P., Torres, O., and Arola, A.: Merging regional and global aerosol
1306   optical depth records from major available satellite products, Atmos. Chem. Phys., 20, 2031–
1307   2056, https://doi.org/10.5194/acp-20-2031-2020, 2020.

1308   Skeie, R. B., Berntsen, T., Myhre, G., Pedersen, C. A., Ström, J., Gerland, S., and Ogren, J.
1309   A.: Black carbon in the atmosphere and snow, from pre-industrial times until present, Atmos.
1310   Chem. Phys., 11, 6809–6836, https://doi.org/10.5194/acp-11-6809-2011, 2011.

1311   Stephens, G. L., and Coauthors,: THE CLOUDSAT MISSION AND THE A-TRAIN: A New
1312   Dimension of Space-Based Observations of Clouds and Precipitation. Bull. Amer. Meteor.
1313   Soc., 83, 1771–1790, https://doi.org/10.1175/BAMS-83-12-1771, 2002.

1314   Stjern, C. W., Samset, B. H., Myhre, G.,Forster, P. M., Hodnebrog, Ø. Andrews,T., Boucher,
1315   O., Faluvegi, G., Iversen, T., Kasoar, M., Kharin, V., Kirkevåg, A., Lamarque, J.-F., Olivie,
1316   D., Richardson, T, Shawki, D., Shindell, D., Smith, C.J., Takemura, T., Voulgarakis, A.
1317   Rapid adjustments cause weak surface temperature response to increased black carbon

concentrations. Journal of Geophysical Research: Atmospheres, 122,11,462–11,481. https://doi.org/10.1002/2017JD02732, 2017.

Stohl, A., Aamaas, B., Amann, M., Baker, L. H., Bellouin, N., Berntsen, T. K., Boucher, O., Cherian, R., Collins, W., Daskalakis, N., Dusinska, M., Eckhardt, S., Fuglestvedt, J. S., Harju, M., Heyes, C., Hodnebrog, Ø., Hao, J., Im, U., Kanakidou, M., Klimont, Z., Kupiainen, K., Law, K. S., Lund, M. T., Maas, R., MacIntosh, C. R., Myhre, G., Myriokefalitakis, S., Olivié, D., Quaas, J., Quennehen, B., Raut, J.-C., Rumbold, S. T., Samset, B. H., Schulz, M., Seland, Ø., Shine, K. P., Skeie, R. B., Wang, S., Yttri, K. E., and Zhu, T.: Evaluating the climate and air quality impacts of short-lived pollutants, Atmos. Chem. Phys., 15, 10529–10566, https://doi.org/10.5194/acp-15-10529-2015, 2015.

Stuecker, M.F., Bitz, C.M., Armour, K.C., Proistosescu, C., Kang, S.M., Xie, S.-P., Kim, D., McGregor, S., Zhang, W., Zhao, S., Cai, W., Dong, Y., Jin, F.-F.: Polar amplification dominated by local forcing and feedbacks, *Nature Climate Change*, 8, 1076–1081, 2018.

Takemura, T., Suzuki, K. Weak global warming mitigation by reducing black carbon emissions. Scientific Reports, 9, 4419 (2019). https://doi.org/10.1038/s41598-019-41181-6

Thomas, J.L., et al.: Fostering multidisciplinary research on interactions between chemistry, biology, and physics within the coupled cryosphere-atmosphere system. Elem Sci Anth, 7: 58. DOI: https://doi.org/10.1525/elementa.396, 2019.

Tsigaridis, K., and M. Kanakidou,: Secondary organic aerosol importance in the future atmosphere. Atmos. Environ., 41, 4682-4692, doi:10.1016/j.atmosenv.2007.03.045, 2007.

Turnock, S. T., Allen, R. J., Andrews, M., Bauer, S. E., Deushi, M., Emmons, L., Good, P., Horowitz, L., John, J. G., Michou, M., Nabat, P., Naik, V., Neubauer, D., O'Connor, F. M., Olivié, D., Oshima, N., Schulz, M., Sellar, A., Shim, S., Takemura, T., Tilmes, S., Tsigaridis, K., Wu, T., and Zhang, J.: Historical and future changes in air pollutants from CMIP6 models, Atmos. Chem. Phys., 20, 14547–14579, https://doi.org/10.5194/acp-20-14547-2020, 2020.

van Marle, M. J. E., Kloster, S., Magi, B. I., Marlon, J. R., Daniau, A.-L., Field, R. D., Arneth, A., Forrest, M., Hantson, S., Kehrwald, N. M., Knorr, W., Lasslop, G., Li, F., Mangeon, S., Yue, C., Kaiser, J. W., and van der Werf, G. R.: Historic global biomass burning emissions for CMIP6 (BB4CMIP) based on merging satellite observations with proxies and fire models (1750–2015), Geosci. Model Dev., 10, 3329–3357, https://doi.org/10.5194/gmd-10-3329-2017, 2017.

Wei, J., Peng, Y., Mahmood, R., Sun, L., and Guo, J.: Intercomparison in spatial distributions and temporal trends derived from multi-source satellite aerosol products, Atmos. Chem. Phys., 19, 7183–7207, https://doi.org/10.5194/acp-19-7183-2019, 2019.

Westervelt, D. M., Horowitz, L. W., Naik, V., Golaz, J.-C., & Mauzerall, D. L.: Radiative forcing and climate response to projected 21st century aerosol decreases. Atmospheric Chemistry and Physics, 15, 12,681– 12,703. https://doi.org/10.5194/acp-15-12681-2015, 2015.

1357   Willis, M. D., Leaitch, W. R., &Abbatt, J. P.: Processescontrolling the composition

1358   andabundance of Arctic aerosol.Reviews of Geophysics, 56, 621–671.

1359   https://doi.org/10.1029/2018RG000602, 2018.

1360   Willmott, C. J. and K. Matsuura,: Terrestrial Air Temperature and Precipitation: Monthly and

1361   Annual Time Series (1950 - 1999), 2001.

1362   (http://climate.geog.udel.edu/~climate/html_pages/README.ghcn_ts2.html, (last access:

1363   October 26th)

Tables

Table 1. GISS-E2.1 simulations carried out in the Eclipse and CMIP6 ensembles.

Simulations	Description	No. Ensemble	Period
NINT_Cpl	No tracers- Coupled	1	1850-2014
Eclipse_AMIP	AMIP OMA	1	1995-2014
Eclipse_AMIP_NCEP	AMIP OMA – winds nudged to NCEP	1	1995-2014
Eclipse_CplHist	OMA – Coupled	3	1990-2014
Eclipse_Cpl_CLE	OMA – Coupled	3	2015-2050
Eclipse_Cpl_MFR	OMA – Coupled	3	2020-2050
CMIP6_Cpl_Hist	OMA – Coupled	1	1850-2014
CMIP6_Cpl_SSP1-2.6	OMA – Coupled	1	2015-2050
CMIP6_Cpl_SSP2-4.5	OMA – Coupled	1	2015-2050
CMIP6_Cpl_SSP3-7.0	OMA – Coupled	1	2015-2050
CMIP6_Cpl_SSP3-7.0-lowNTCF	OMA – Coupled	1	2015-2050

Table 2. Annual mean normalized mean bias (*NMB:%*) and correlation coefficients (*r*) for the recent past simulations in the GISS-E2.1 model ensemble during 1995-2014 for BC, OA, SO_4^{2-} and 2008/2009-2014 for AOD550 from AERONET and satellites.

	BC		OA		SO_4^{2-}		AOD_aero		AOD_sat	
Model	*NMB*	*r*	*NMB*	*r*	*NMB*	*r*	*NMB*	*r*	*NMB*	*r*
AMAP_OnlyAtm.	-67.32	0.27	-35.46	0.54	-49.83	0.65	-33.28	-0.07	-0.48	0.00
AMAP_OnlyAtm_NCEP	-57.00	0.26	-7.80	0.56	-52.70	0.74	-41.99	0.02	-0.55	0.13
AMAP_CplHist (x3)	-64.11	0.42	-19.07	0.58	-49.39	0.71	-43.28	0.04	-0.56	0.07
CMIP6_Cpl_Hist	-49.90	0.26	13.14	0.69	-39.81	0.70	-39.86	0.05	-0.53	0.11

Table 3a. Annual normalized mean biases (*NMB*: %) and correlation coefficients (*r*) for the recent past simulations in the GISS-E2.1 model ensemble in 1995-2014 for surface air temperature (T_{surf}) and sea surface temperature (SST) in units of °C, and precipitation (Precip), and sea-ice fraction (Sea-ice).

	T_{surf}		Precip		SST		Sea-ice	
Model	*NMB*	*r*	*NMB*	*r*	*NMB*	*r*	*NMB*	*r*
NINT	-0.08	1.00	-52.68	0.88	-88.87	0.99	12.14	1.00
AMAP_OnlyAtm.	-19.73	1.00	-50.33	0.89	-68.00	0.99	-2.56	1.00
AMAP_OnlyAtm_NCEP	-14.74	1.00	-53.19	0.90	-68.00	0.99	-2.56	1.00
AMAP_CplHistx3	-3.35	1.00	-53.06	0.86	-87.51	0.99	11.35	1.00
CMIP6_Cpl_Hist	-1.22	1.00	-53.96	0.85	-88.53	0.98	12.56	0.99

Table 3b. Annual mean normalized mean biases (*NMB*: %) and correlation coefficients (*r*) for the recent past simulations in the GISS-E2.1 model ensemble in 1995-2014 for total cloud fraction (Cld Frac), liquid water path (LWP), and ice water path (IWP) in units of %.

	Cld Frac		LWP		IWP	
Model	*NMB*	*r*	*NMB*	*r*	*NMB*	*r*
NINT	20.95	-0.67	70.55	-0.89	-56.06	0.53
AMAP_OnlyAtm.	23.78	-0.81	57.52	-0.96	-58.53	-0.18
AMAP_OnlyAtm_NCEP	24.83	-0.79	14.19	-0.91	-70.32	-0.64
AMAP_CplHistx3	21.64	-0.65	70.99	-0.91	-55.74	0.48
CMIP6_Cpl_Hist	21.49	-0.65	69.18	-0.91	-56.28	0.40

Table 4. Trends in Arctic BC, OA and SO_4^{2-} burdens in the near-past (1990-2014) and future (2030-2050) as calculated by the GISS-E2.1. The bold numbers indicate the trends that are statistically significant on a 95% significance level.

	BC		OA		SO_4^{2-}	
	1990-2014	2015-2050	1990-2014	2015-2050	1990-2014	2015-2050
Eclipse_AMIP	**-0.026**		0.030		**-0.886**	
Eclipse_AMIP_NCEP	**-0.021**		0.112		**-0.939**	
Eclipse_CplHist_3xEns	**-0.026**		-0.006		**-1.332**	
Eclipse_CplCLE_3xEns		**-0.024**		**-0.201**		**-0.143**
Eclipse_CplMFR_3xEns		**-0.043**		**-0.367**		**-0.146**
CEDS_Cpl_Hist	0.007		0.121		**-1.093**	
CEDS_Cpl_SSP126		**-0.068**		**-0.715**		**-0.935**
CEDS_Cpl_SSP245		**-0.047**		**-0.384**		**-0.465**
CEDS_Cpl_SSP370		**-0.004**		**-0.062**		**0.027**
CEDS_Cpl_SSP370-lowNTCF		**-0.051**		**-0.642**		**-0.567**

Table 5. Arctic BC, OA and SO_4^{2-} burdens in 1990-2010 and 2030-2050 periods as calculated by the GISS-E2.1.

	BC		OA		SO_4^{2-}	
	1990-2010	2030-2050	1990-2010	2030-2050	1990-2010	2030-2050
Eclipse_AMIP	3.52		50.70		95.10	
Eclipse_AMIP_NCEP	3.49		57.31		93.93	
Eclipse_CplHist_3xEns	3.75		55.55		93.59	
Eclipse_CplCLE_3xEns		2.58		48.95		63.52
Eclipse_CplMFR_3xEns		1.44		40.39		53.35
CEDS_Cpl_Hist	3.64		67.48		99.11	
CEDS_Cpl_SSP126		2.05		50.41		53.99
CEDS_Cpl_SSP245		2.65		59.43		69.71
CEDS_Cpl_SSP370		4.08		68.81		83.26
CEDS_Cpl_SSP370-lowNTCF		2.94		56.05		69.72

Table 6a. RF$_{ARI}$ for BC, OA, SO$_4^{2-}$ and NO$_3^-$ aerosols in 1990-2010 and 2030-2050 periods as calculated by the GISS-E2.1.

	BC		OA		SO$_4^{2-}$		NO$_3^-$	
	1990-2010	2030-2050	1990-2010	2030-2050	1990-2010	2030-2050	1990-2010	2030-2050
NINT_Cpl	0.20		-0.05		-0.33		-0.01	
Eclipse_AMIP	0.20		-0.06		-0.39		-0.02	
Eclipse_AMIP_NCEP	0.19		-0.08		-0.39		-0.04	
Eclipse_CplHist_3xEns	0.23		-0.05		-0.38		-0.03	
Eclipse_CplCLE_3xEns		0.17		-0.07		-0.27		-0.07
Eclipse_CplMFR_3xEns		0.09		-0.07		-0.22		-0.04
CEDS_Cpl_Hist	0.23		-0.06		-0.40		-0.04	
CEDS_Cpl_SSP126		0.13		-0.07		-0.22		-0.10
CEDS_Cpl_SSP245		0.19		-0.08		-0.29		-0.09
CEDS_Cpl_SSP370		0.28		-0.09		-0.34		-0.06
CEDS_Cpl_SSP370-lowNTCF		0.20		-0.07		-0.28		-0.09

Table 6b. RF$_{ARI}$ for total and anthropogenic aerosols in 1990-2010 and 2030-2050 periods as calculated by the GISS-E2.1.

	Aerosols Total		Anthropogenic Aerosols	
	1990-2010	2030-2050	1990-2010	2030-2050
NINT_Cpl	-0.35		-0.19	
Eclipse_AMIP	-0.46		-0.27	
Eclipse_AMIP_NCEP	-0.47		-0.32	
Eclipse_CplHist_3xEns	-0.32		-0.22	
Eclipse_CplCLE_3xEns		-0.39		-0.24
Eclipse_CplMFR_3xEns		-0.39		-0.23
CEDS_Cpl_Hist	-0.35		-0.26	
CEDS_Cpl_SSP126		-0.40		-0.26
CEDS_Cpl_SSP245		-0.41		-0.27
CEDS_Cpl_SSP370		-0.35		-0.21
CEDS_Cpl_SSP370-lowNTCF		-0.38		-0.24

Table 7. Trends in near surface temperature (T_{surf}) and annual mean sea-ice extent in 1990-2010 and 2030-2050 periods as calculated by the GISS-E2.1. The bold numbers indicate the changes in 2030-2050 mean compared to the 1990-2010 mean that are statistically significant on a 95% significance level.

	T_{surf} (°C decade^{-1})		Sea-ice (10^3 km^2)	
	1990-2010	2030-2050	1990-2010	2030-2050
Observed	**0.19**		**-28.36**	
NINT_Cpl	**0.88**		**-60.10**	
Eclipse_AMIP	**0.52**		**-28.65**	
Eclipse_AMIP_NCEP	**0.62**		**-29.47**	
Eclipse_CplHist_3xEns	**0.52**		**-37.89**	
Eclipse_CplCLE_3xEns		**0.45**		**-37.212**
Eclipse_CplMFR_3xEns		**0.55**		**-41.33**
CEDS_Cpl_Hist	**0.10**		**-69.79**	
CEDS_Cpl_SSP126		**0.31**		**-23.21**
CEDS_Cpl_SSP245		**0.38**		**-24.28**
CEDS_Cpl_SSP370		**0.50**		**-39.18**
CEDS_Cpl_SSP370-lowNTCF		**0.31**		**-21.89**

Table 8. Near surface temperature (T_{surf}) and September-mean sea-ice extent in 1990-2010 and 2030-2050 periods as calculated by the GISS-E2.1. The bold numbers indicate the changes in 2030-2050 mean compared to the 1990-2010 mean that are statistically significant on a 95% significance level.

	T_{surf} (°C)		September Sea-ice (10^3 km^2)	
	1990-2010	2030-2050	1990-2010	2030-2050
NINT_Cpl	-8.39			
Eclipse_AMIP	-6.54			
Eclipse_AMIP_NCEP	-7.10			
Eclipse_CplHist_3xEns	-8.13		1.56	
Eclipse_CplCLE_3xEns		**-6.06**		**1.32**
Eclipse_CplMFR_3xEns		**-5.79**		**1.31**
CEDS_Cpl_Hist	-8.52		1.60	
CEDS_Cpl_SSP126		**-6.64**		1.44
CEDS_Cpl_SSP245		**-6.37**		1.37
CEDS_Cpl_SSP370		**-6.33**		1.37
CEDS_Cpl_SSP370-lowNTCF		**-6.56**		1.38

Figures
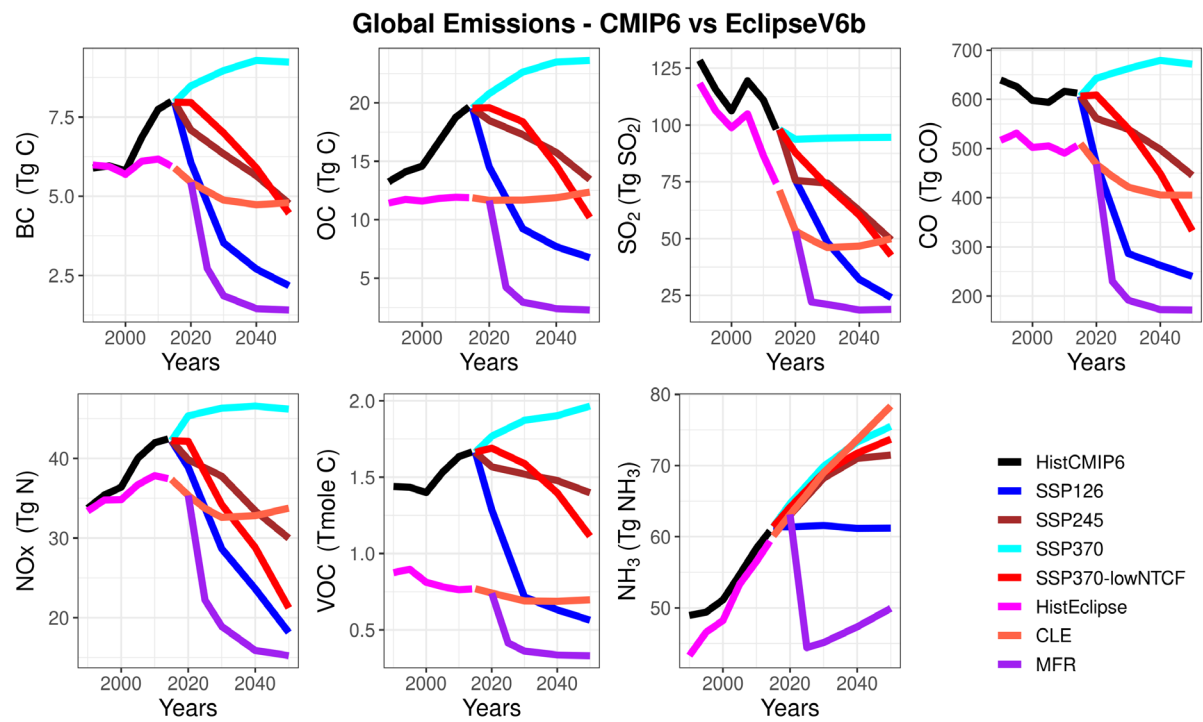
Figure 1. Global recent past and future CMIP6 and Eclipse V6b anthropogenic emissions for different pollutants and scenarios.
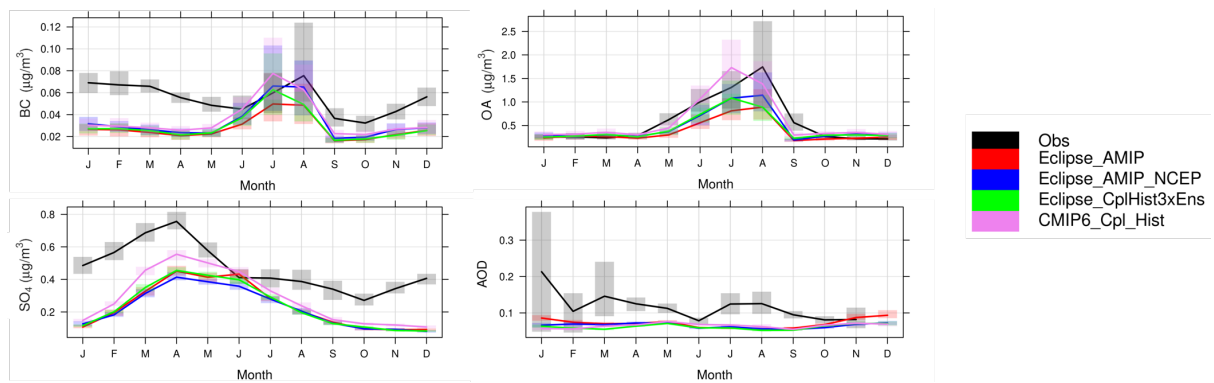
Figure 2. Observed and simulated Arctic climatological (1995-2014) monthly BC, OA, SO_4^{2-}, and AERONET AOD at 550nm (2008/09-14), along with the interannual variation shown in bars. The data presents monthly accumulated timeseries for all stations that are merged together.
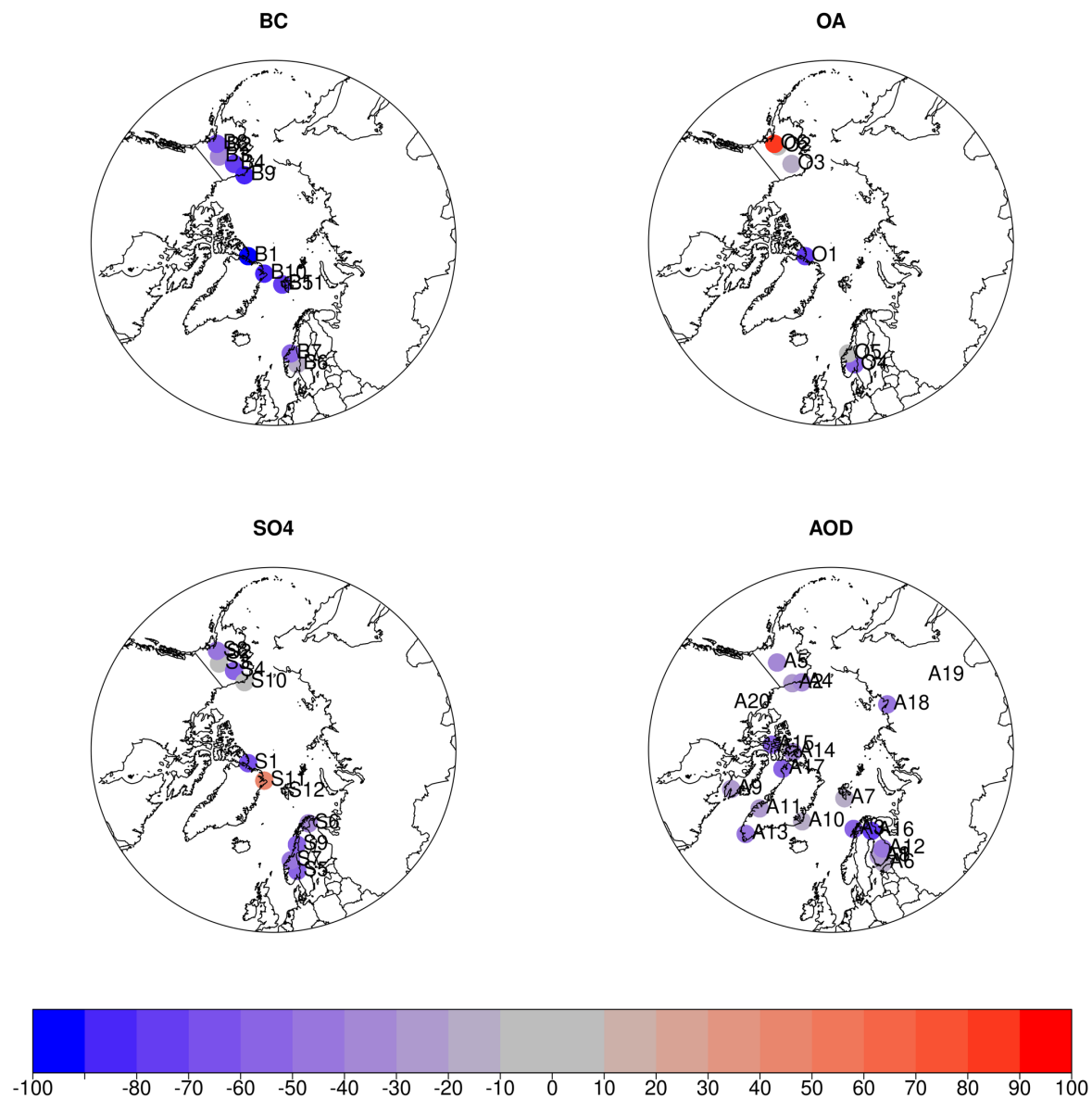
Figure 3. Spatial distribution of normalized mean bias (*NMB*, in %) for climatological mean (1995-2014) BC, OA, SO$_4^{2-}$ and AOD at monitoring stations, calculated as the mean of all recent past simulations.
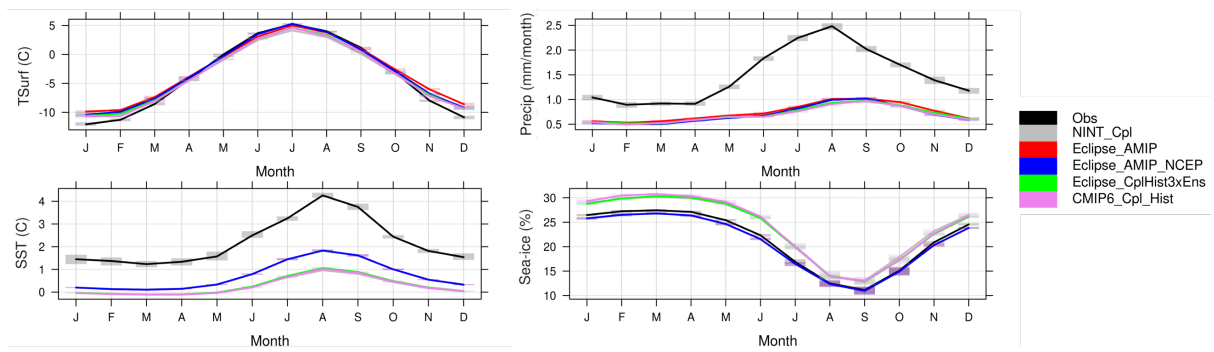
Figure 4. Observed and simulated Arctic climatological (1995-2014) surface air temperature, precipitation, sea surface temperature, and sea-ice, along with the interannual variation shown in bars. Obs denote UDel dataset for surface air temperature and precipitation, and HADISST for sea surface temperature and sea-ice extent. Note that the two AMIP runs (blue and red lines) for the SST and sea-ice are on top of each other as they use that data to run, as input.
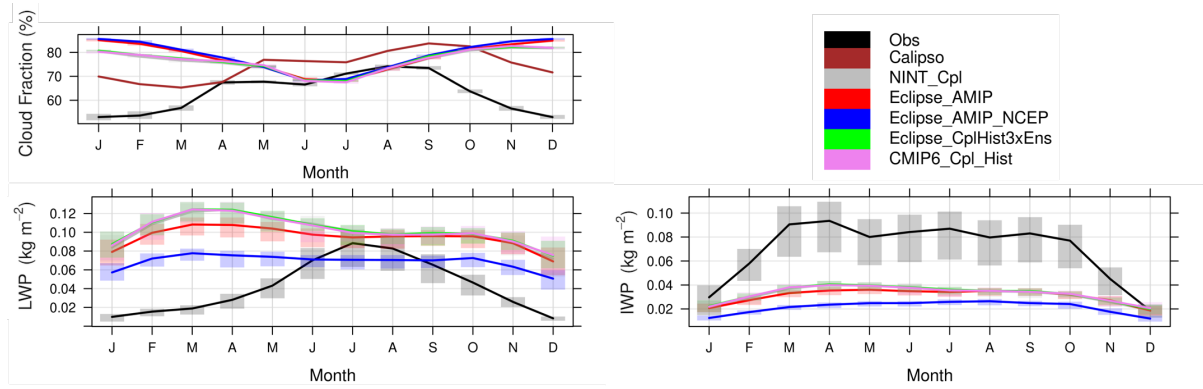
Figure 5. Observed and simulated Arctic climatological total cloud fraction (1995-2014 mean), liquid water path (2007-2014 mean), and ice water path (2007-2014 mean) , along with the interannual variation shown in bars. Obs denote Clara-A2 for the cloud fractions and CloudSat for the LWP and IWP.
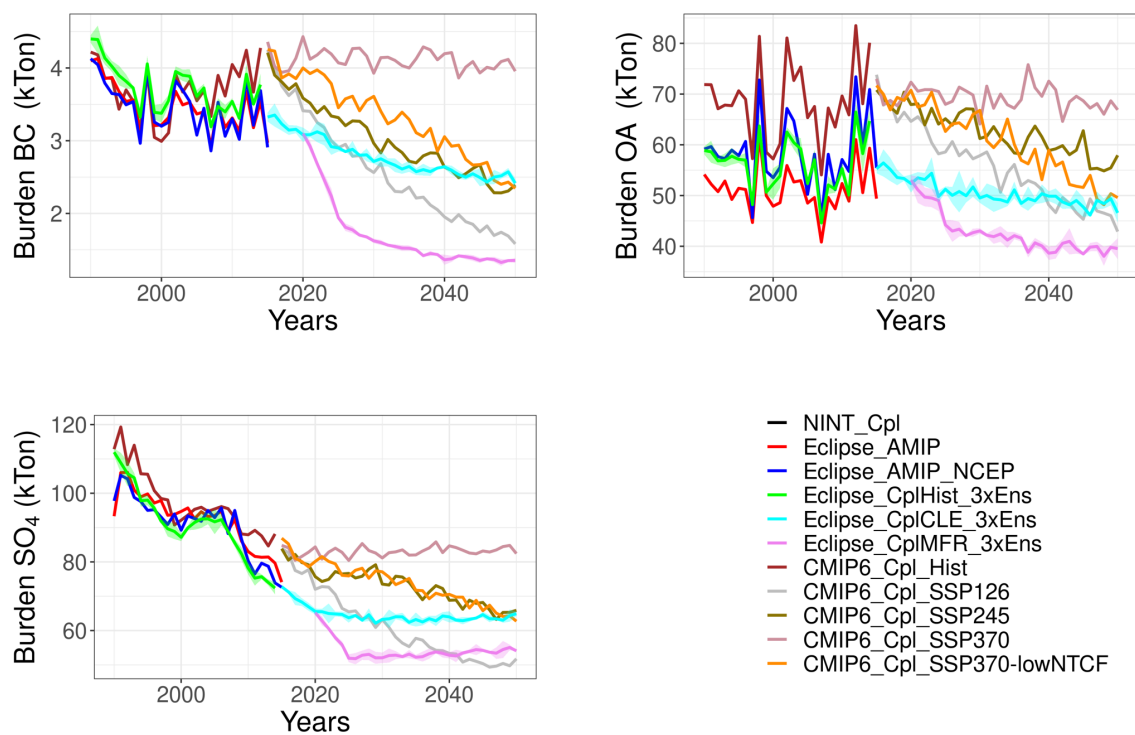
Figure 6. Arctic BC, OA and SO4²⁻ burdens in 1990-2050 as calculated by the GISS-E2.1 ensemble.
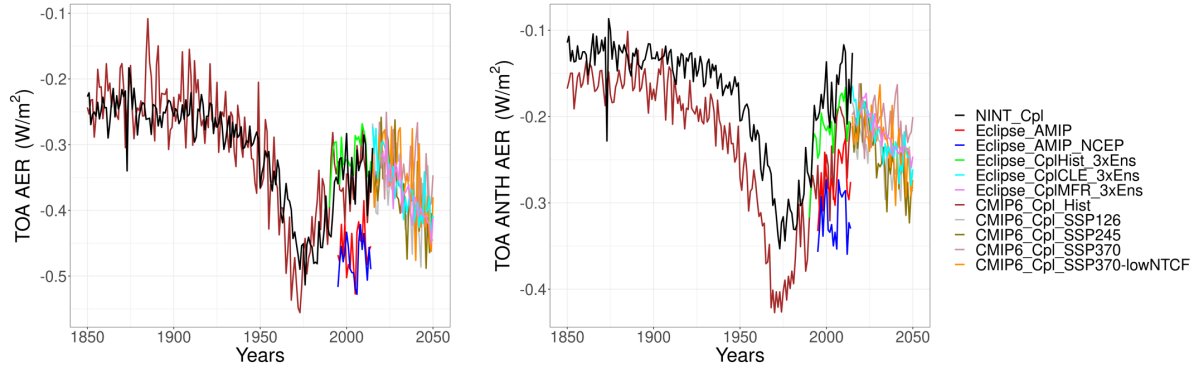
Figure 7. Arctic RF$_{ARI}$ from anthropogenic and natural aerosols (BC+OA+SO$_4^{2-}$+NO$_3^-$+Dust+SSA), and only anthropogenic aerosols (BC+OA+SO$_4^{2-}$+NO$_3^-$) in 1850-2050 as calculated by the full GISS-E2.1 ensemble.
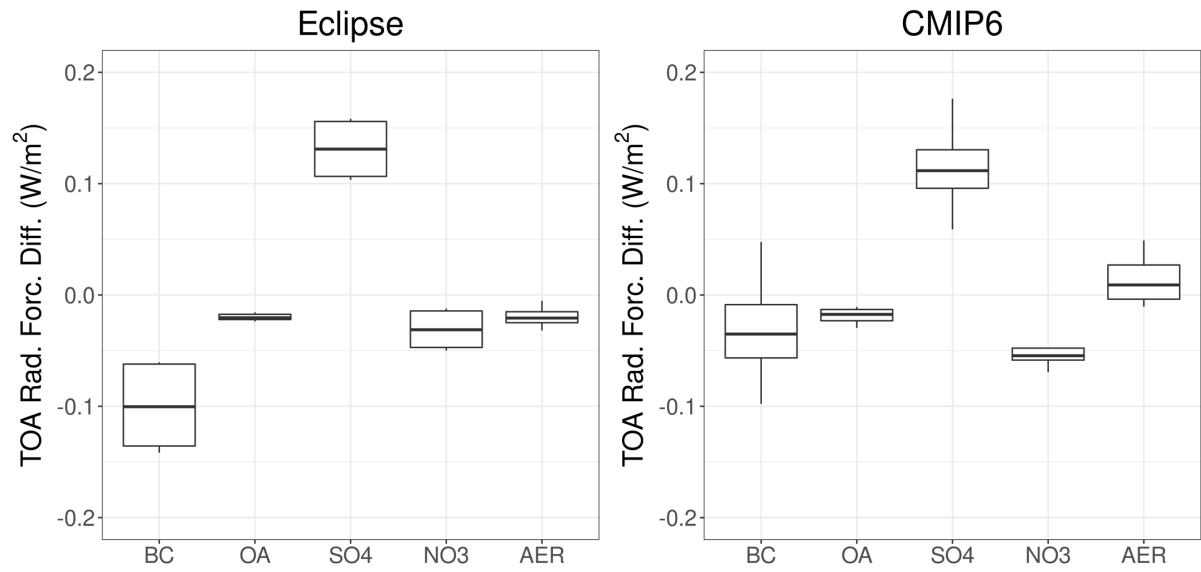
Figure 8. Box-Whisker plot showing the differences between 1990-2010 mean and 2030-2050 mean RF_{ARI} for the anthropogenic aerosol components (BC, OA, SO_4^{2-} and NO_3^-) and their sum (AER) in the Eclipse (left panel) and the CMIP6 (right panel) ensembles. The boxes show the median, the 25th and 75th percentiles. The upper whisker is located at the *smaller* of the maximum value and $Q\_3 + 1.5$ IQR, whereas the lower whisker is located at the *larger* of the smallest x value and $Q\_1 – 1.5$ IQR, where IQR (interquartile range) is the box height (75th percentile - 25th percentile).
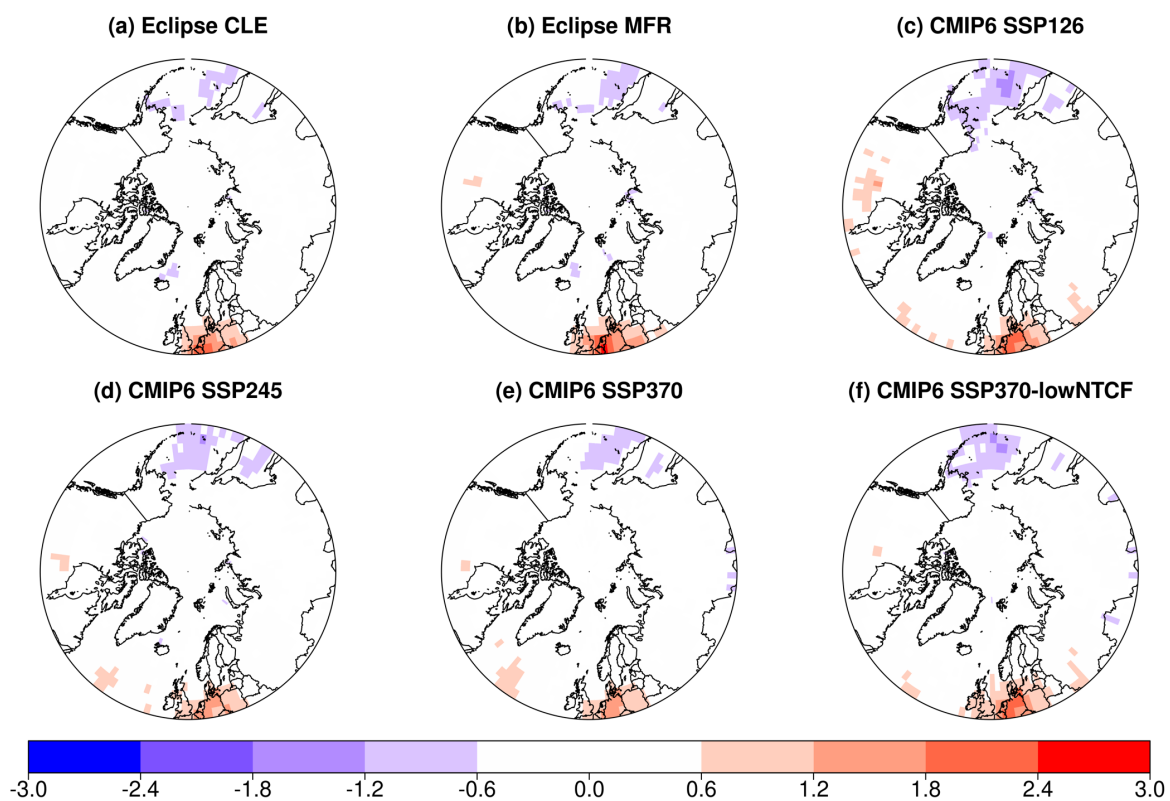
Figure 9. Spatial distribution of the statistically significant annual mean Arctic RF_{ARI} (W m^{-2}) changes between the 1990-2010 mean and the 2030-2050 mean as calculated by the GISS-E2.1 ensemble.
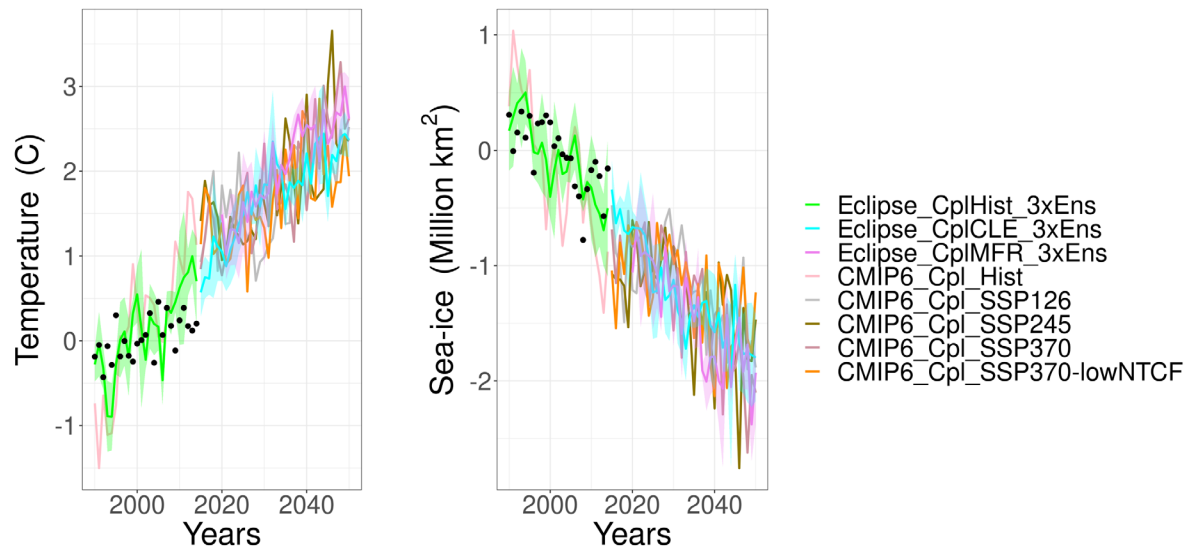
Figure 10. Arctic annual mean surface air temperature and sea-ice extent anomalies in 2015-2050 based on the 1990-2010 mean as calculated by the GISS-E2.1 ensemble.
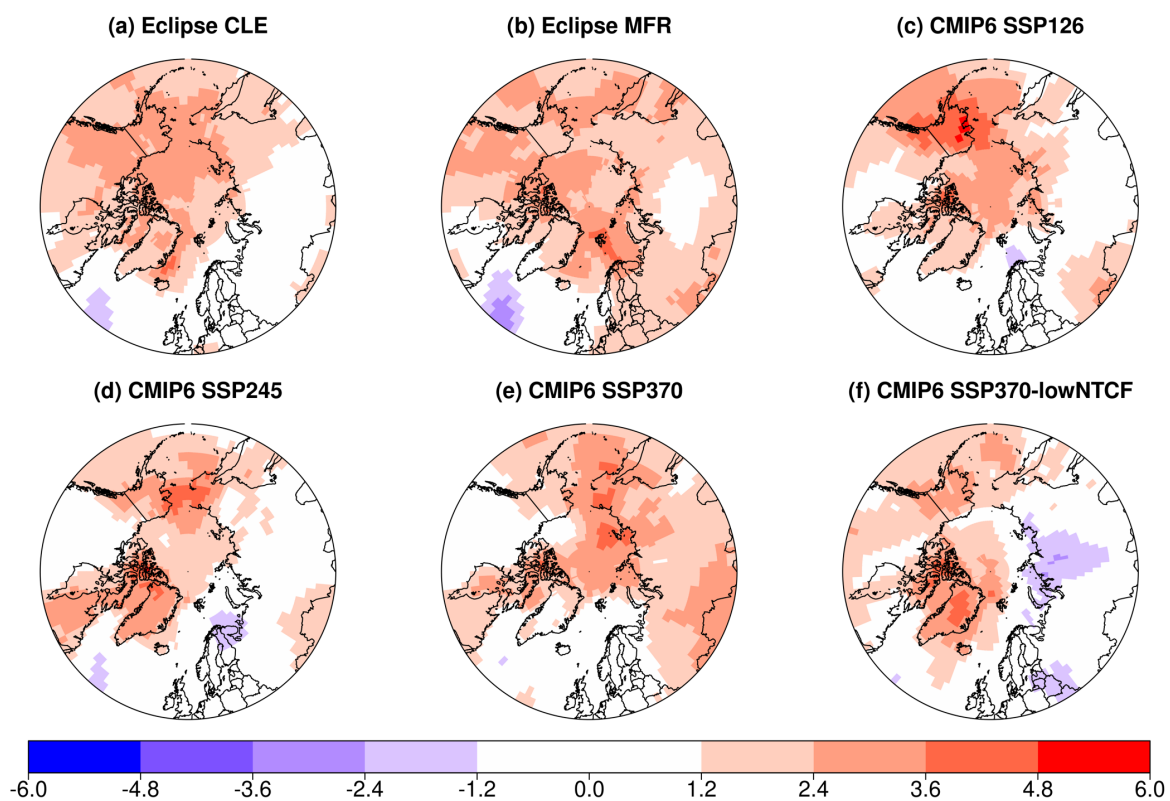
Figure 11. Spatial distribution of the statistically significant annual mean Arctic surface air temperature (°C) changes between the 1990-2010 mean and the 2030-2050 mean as calculated by the GISS-E2.1 ensemble.

(a) Eclipse CLE   **(b) Eclipse MFR**
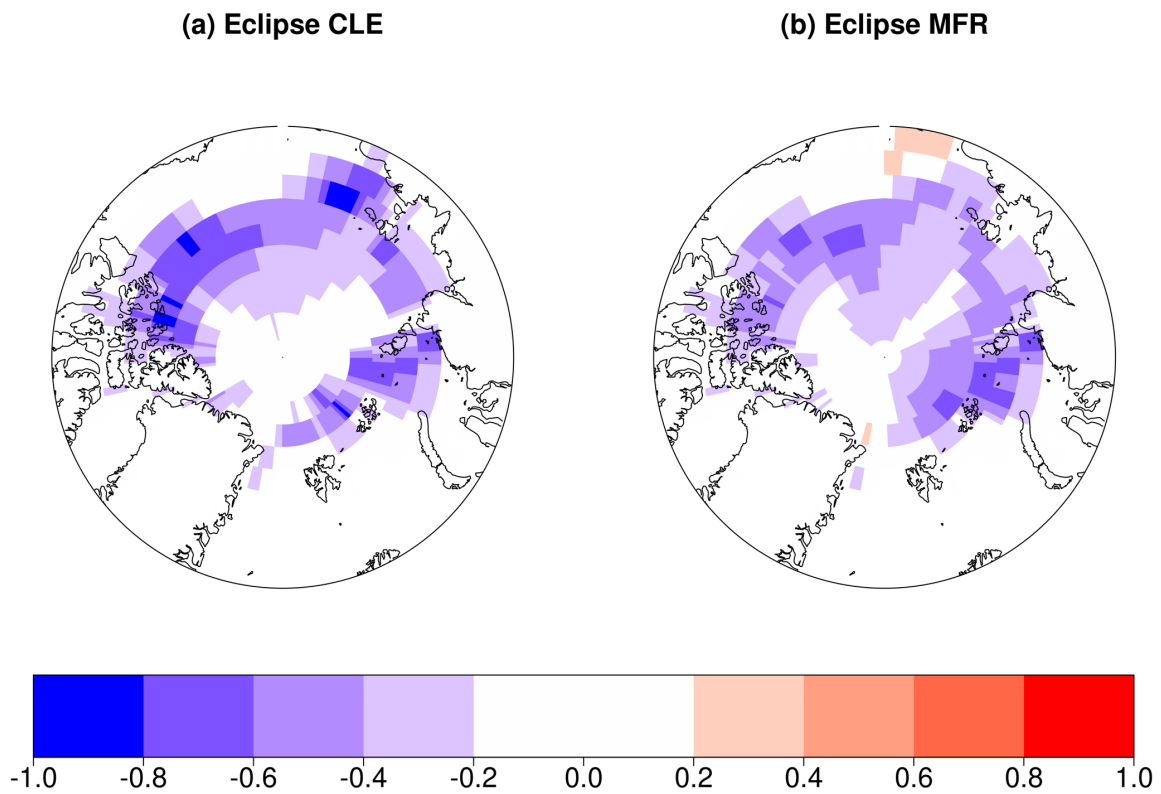
Figure 12. Spatial distribution of the statistically significant September Arctic sea-ice fraction change between the 1990-2010 mean and the 2030-2050 mean as calculated by the GISS-E2.1 Eclipse ensemble (CMIP6 ensemble is not shown due to statistically insignificant changes calculated by the student t-test).